



HAL
open science

Hectorite: Synthesis, modification, assembly and applications

Jing Zhang, Chun Hui Zhou, Sabine Petit, Hao Zhang

► **To cite this version:**

Jing Zhang, Chun Hui Zhou, Sabine Petit, Hao Zhang. Hectorite: Synthesis, modification, assembly and applications. Applied Clay Science, 2019, 177, pp.114-138. 10.1016/j.clay.2019.05.001 . hal-02363196

HAL Id: hal-02363196

<https://cnrs.hal.science/hal-02363196v1>

Submitted on 2 Dec 2020

HAL is a multi-disciplinary open access archive for the deposit and dissemination of scientific research documents, whether they are published or not. The documents may come from teaching and research institutions in France or abroad, or from public or private research centers.

L'archive ouverte pluridisciplinaire **HAL**, est destinée au dépôt et à la diffusion de documents scientifiques de niveau recherche, publiés ou non, émanant des établissements d'enseignement et de recherche français ou étrangers, des laboratoires publics ou privés.

1 Hectorite: Synthesis, Modification, Assembly and Applications

2
3 Jing Zhang^a, Chun Hui Zhou^{a,b,c*}, Sabine Petit^d, Hao Zhang^a

4
5 ^a Research Group for Advanced Materials & Sustainable Catalysis (AMSC), State Key Laboratory
6 Breeding Base of Green Chemistry-Synthesis Technology, College of Chemical Engineering, Zhejiang
7 University of Technology, Hangzhou 310032, China

8 ^b Key Laboratory of Clay Minerals of Ministry of Land and Resources of the People's Republic of
9 China, Engineering Research Center of Non-metallic Minerals of Zhejiang Province, Zhejiang Institute
10 of Geology and Mineral Resource, Hangzhou 310007, China

11 ^c Qing Yang Institute for Industrial Minerals, You Hua, Qing Yang, Chi Zhou 242804, China

12 ^d Institut de Chimie des Milieux et Matériaux de Poitiers (IC2MP), UMR 7285 CNRS, Université de
13 Poitiers, Poitiers Cedex 9, France

14
15 Correspondence to: Prof. CH Zhou E-mail: clay@zjut.edu.cn; chc.zhou@aliyun.com

18 **Abstract**

19
20 Hectorite ($\text{Na}_{0.6}\text{Mg}_{2.7}\text{Li}_{0.3}\text{Si}_4\text{O}_{10}(\text{OH})_2$) is a trioctahedral clay mineral with peculiar cation
21 exchange capacity, surface reactivity and adsorption, and easy delamination in water into
22 individual nanolayers, which can then re-assemble in various ways. The aqueous dispersion of
23 hectorite exhibits exclusive rheological and thixotropic properties. The paper reviews recent
24 progress in the synthesis, modification, assembly and applications of hectorite. The present
25 methods for synthesizing hectorite are hydrothermal synthesis, melt synthesis and
26 structure-directed synthesis. Modification of hectorite can be made by ion exchange, intercalation,
27 pillaring and grafting. Layer-by-layer assembly, template assembly and hierarchical assembly
28 have been used to form a variety of hectorite-containing hybrids and nanocomposites such as
29 films, membranes, capsules and Janus nanoparticles. Hectorite and hectorite-derived materials can
30 be used as adsorbents, catalysts, fluorescent reporters, hydrogels, and biomaterials. Literature
31 survey has indicated that hectorite has been successfully used as rheological and thixotropic
32 materials, and are being developed to be used in battery, fluorescent reporters, drug vehicles and
33 tissue engineering.

34 **Keywords:** Hectorite; Synthesis; Modification; Assembly; Adsorption; Hydrogel; Biomaterials

36 **1. Introduction**

37 Hectorite is a natural layered magnesium-lithium silicate, and it is a trioctahedral clay
38 mineral with an ideal chemical formula of $\text{Na}_{0.6}\text{Mg}_{2.7}\text{Li}_{0.3}\text{Si}_4\text{O}_{10}(\text{OH})_2$ in the smectite group. The
39 layered structure of hectorite is composed of Si-O-Mg(Li)-O-Si- layers separated by hydrated
40 cations (e.g. Na^+ , Li^+) in the interlayer space. Each layer (ca. 0.96 nm thin) consists of two
41 Si-O-Si tetrahedral sheets sandwiching a Mg-O-Li octahedral sheet in a so-called 2:1 arrangement
42 (**Fig. 1a**). The adjacent negatively-charged 2:1 layer is fixed by positively-charged interlayer
43 cations and by hydrogen bonding between water molecules coordinated to interlayer cations and
44 basal oxygen atoms of tetrahedral sheets. The partly isomorphous substitution of Li^+ for Mg^{2+} in
45 the octahedral sheets cause negative charges that is compensated by interlayer cations in the

46 interlayer space and the interlayer cations are exchangeable. Hectorite nanolayers possess
47 anisotropic distribution of charge in the layer: negative charges on the basal faces and positive
48 charges on the edges (**Fig. 1a**). The amphoteric groups (Mg-O, Li-O, and Si-O) at the broken edge
49 of the crystals is protonated (Mg-OH_2^+ , Li-OH_2^+ , and Si-OH_2^+) or deprotonated (Mg-O^- , Li-O^- ,
50 and Si-O^-), depending on the pH (Bourlinos et al., 2004). Hectorite has cation exchange capacity
51 (CEC) ranged from 50 to 150 mmol/100g over the pH range of 6 to 13 (Delavernhe et al., 2018),
52 and specific surface area about $350\text{m}^2/\text{g}$ (Hegyesei et al., 2017).

53

54

Fig. 1.

55

56 Hectorite can spontaneously swelling and then delaminate in water (Gaharwar et al., 2013).
57 Many dispersed individual layers in water can then form the structure of “house-of-cards” (Fig.
58 1b). Such randomly oriented “house-of-cards”, and t stacking can be destroyed and aligned under
59 a shearing force. Under static condition, an aqueous dispersion of delaminated hectorite can form
60 sol or hydrogel with a 3D network, primarily dependent on the concentration, media and electrolyt
61 (Iwase et al., 2018; Lezhnina et al., 2012). As such, the aqueous dispersion of hectorite exhibits
62 superior and tunable rheological and thixotropic properties (Phuoc et al., 2009; Tan et al., 2014).

63

64 Hectorite deposits in nature are rare. Due to the geological environments and conditions,
65 natural hectorite at different deposits has variable crystallinity and various impurities, limiting the
66 use of hectorite. Hectorite is one of easily synthesized clay minerals by a hydrothermal process in
67 the laboratory and in industry (Strese and Hofmann, 1941; Granquist and Pollack, 1959;
68 Decarreau, 1980; Zhang et al, 2010). Laponite[®], a kind of synthetic hectorite, has been produced
69 on a large scale and widely used (The name Laponite[®] was introduced by the Laporte Industries
70 decade ago). Ideally, well-synthetic hectorite is homogeneous in composition and crystallinity by
71 controlling the hydrothermal process. Besides, studies have indicated that hectorite-like solid can
72 be synthesized by a solid-state reaction or template synthesis. In this way, the nanolayer can be
73 controlled to have a high aspect ratio or to be conducive to form porous structure. In addition, the
74 reactive groups on the surface and the edge of hectorite allow hectorite to be functionalized by
grafting. The functionalized hectorite can be further assembled with other molecules and

75 nanomaterials to form nanohybrids or nanocomposites by layer-by-layer assembly, template
76 assembly or hierarchical assembly.

77 New discoveries and technologies about hectorite emerged constantly, and one can say that
78 the excitement of hectorite continues unabated in the recent decade (**Fig. 2a**). Traditionally,
79 hectorite can be used as adsorbent, catalytic and rheological additives. More recently, hectorite is
80 often seen to be used in the fields of advanced analytic and optical, diagnostic, medical materials
81 and tissue engineering (**Fig. 2b**). In particular, new technologies for synthesis, modification and
82 assembly of hectorite is paving the way for many new applications of hectorite.

83

84

Fig.2.

85

86 **2. Synthesis**

87 **2.1 Hydrothermal synthesis**

88 Since Strese and Hofmann (1941) successfully synthesized hectorite-like solid from aqueous
89 solution at reflux temperature for the first time, a hydrothermal process has been commonly used
90 for synthesizing hectorite (**Table 1**). Though this technology of synthesis of hectorite has become
91 much mature, cleaner production of hectorite with more energy-efficiency is still need. In addition,
92 synthetic hectorite with new structures such as ordered heterostructures (Stöter et al., 2014) and
93 Janus nanoparticles (Stöter et al., 2016) also rekindles the development of the methods to
94 synthesize hectorite.

95

96

Table 1

97

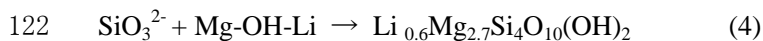
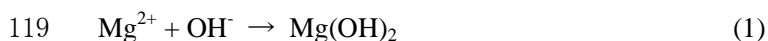
98 **2.1.1 Formation mechanism**

99 It has been generally believed that hectorite. nucleation is initiated from brucite sheets. To be
100 specific, the nuclei occur starting with the condensation of silicate tetrahedral Si-O blocks onto

101 brucite sheets (**Fig. 3a, eq 1**). It has been ever observed that during the synthesis, the more
 102 crystalline brucite is yielded, the larger amount of crystalline hectorite is produced (Vicente et al.,
 103 2009). In addition, it is found that some of these initial nuclei are redissolved and recondensed to
 104 form nuclei of hectorite (Okada et al., 2012; Okada et al., 2015a; Okada et al., 2016b). In the
 105 process, the added Mg^{2+} and Li^+ form water-soluble Mg-Li double hydroxide (**Fig. 3c, eq 3**). Such
 106 brucite-like Mg-Li sheets act as initial species for nucleation and growth. The sheets are also the
 107 precursors of the octahedral sheet of the resultant hectorite.

108 The silica (SiO_2) on the surface of SiO_2 precipitates or solids dissolves into the aqueous phase
 109 to form silicate anions SiO_3^{2-} (**Fig. 3b, eq 2**) When approaching the Mg-Li hydroxide, the silicate
 110 anions condense and meanwhile react with on the Mg-Li double hydroxide to form nuclei. During
 111 nucleation and growth of hectorite, dehydroxylation mainly occurs. Finally, the nuclei and tiny
 112 crystallite of 2:1 layered Mg-Li-silicates, namely hectorite, grows in a two-dimensional way (**Fig.**
 113 **3d, eq 4**). The dissolved silica is continuously consumed with the formation of hectorite. The
 114 compositional balance of silica, LiF, and $MgCl_2$ should be responsible for the heterogeneous
 115 nucleation (Okada et al., 2015b; Okada et al., 2016a). Whatever the process involved, after the
 116 crystallization is complete, layer-layer stacking and agglomeration of nanoparticles takes place
 117 commonly (Carrado et al., 2002).

118



123

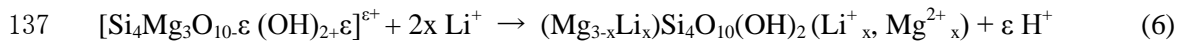
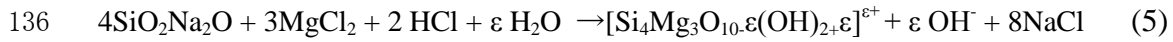
124 **Fig.3.**

125

126 Yet it is worth arguing if the preceding formation of brucite sheet are necessary step in the
 127 formation of hectorite. For example, A process using coprecipitated gels (**eq 5**) with further or
 128 immediate addition of LiF (or LiCl) (**eq 6**) followed by hydrothermal treatment also produced
 129 hectorite (Decarreau, 1980; Decarreau et al., 2012). In the studies, freshly coprecipitated gels

130 appeared to contain nanoparticles (less than 0.1 μm in diameter) and the nanoparticles aggregated
131 more or less. The freshly coprecipitated gels were composed of nuclei which had the structure of
132 hectorite layers (Decarreau, 1980). OH^- released during reaction (eq 5). Owing to H^+ release into
133 solution (eq 6), a decrease of pH with the time of hydrothermal treatment. After reaction of
134 nucleation, the pH was between 9 and 10 (Carrado, 2000)

135



138

139 F^- ions are viewed as favorable mineralizing agents during the hydrothermal synthesis of
140 hectorite. Such mineralizing agents could play a role in regulating dissolution, hydrolysis,
141 condensation, dehydroxylation and thereby nucleation and growth of hectorite crystals. In
142 particular, it has been suggested that F^- ions promote the dissolution and hydrolysis of the silica
143 (Okada et al., 2015a). Moreover, it has been revealed that the F^- ions partly replaced the hydroxyl
144 groups in the layer and created defects in the lattice (Jaber and Miehé-Brendlé, 2008). Such F^- in
145 the framework of hectorite layers inhibit the interaction of neighboring hydroxyls to produce water,
146 as proved by the enhanced thermal stability of fluorohectorite. Finally, it is also revealed that the
147 presence of F^- ions during the synthesis resulted in enhanced layer stacking in the direction of the
148 c^* -axis in the heterogeneous nucleation and growth of hectorite (Okada et al., 2015a).

149

150 **2.1.2. Insights into reaction conditions**

151 The composition and purity of synthetic hectorite can be controlled by judiciously choosing
152 the molar ration of Si:Mg:Li and the hydrothermal reaction conditions (Zhou et al., 2010). The
153 size distribution of synthetic hectorite, which is inherently to the nucleation and growth of
154 synthetic hectorite crystals, can also be tuned primarily by crystallization time, hydrothermal
155 temperature, pH value and heating. It is also influenced by the methods of heating and stirring, for
156 example microwave heating and ultrasonication (Table 1).

157 Synthetic hectorite is usually produced from crystallizing an aqueous mixture of LiF and/or
158 LiCl, Mg(OH)₂ and SiO₂ at high-temperature under reflux conditions in an open system or under
159 autogenic pressure in an autoclave. Generally, the molar ratio of reactants for synthetic hectorite is
160 set to match the ideal composition of natural hectorite Na_{0.66}[Li_{0.66}Mg_{5.34}Si₈O₂₀(OH)₄]. But the
161 ions from the reactants might play a multiple role in the formation of hectorite. Typically, Li⁺
162 substitute for some of octahedral Mg²⁺, leading to layer charge (Makoto et al., 2008). Decarreau et
163 al. (2012) recently revealed that the Li content of hectorite increased with the Li⁺ concentration in
164 the solution and proposed a partition coefficient D_{Li} with a general expression $D_{Li} =$
165 $\frac{Li_{hectorite}}{Li_{solution}}$ and $\text{Log } D_{Li} = -1.319 \cdot 10^3/T + 5.5 (Li_{solution})^{-0.0806}$ (T=343-453K).
166 Accordingly, the Li/Mg molar ratio of reactants significantly influence the layer charge density
167 (LCD) and the CEC due to the variable isomorphous substitution (Karmous et al., 2009; Okada et
168 al., 2015b). In addition, it has been found that the amount of LiF can also affect the size of the
169 hectorite crystals, the surface area and pore size of the synthetic hectorite (Pawar et al., 2013).

170 Various metal-substituted hectorite-like solid have been synthesized (**Table 1**).
171 Well-crystallized Zn-hectorite (Na_{0.4} (Li_{0.4}Zn_{2.6})Si₄O₁₀(OH)₂·nH₂O) were obtained at 373K
172 (Spagnuolo, 2004). Cu, Ni, Mn and Co-hectorite can only be hydrothermally synthesized under
173 the conditions of more crystallization time and higher temperature (around 473K) (Spagnuolo,
174 2004), due to the lower electronegativity (Ni, Mn and Co electronegativity: 1.91;1.55;1.8)
175 (Higashi et al., 2007). The electronegativity of ions is directly related to the ionic radius. Besides,
176 actinides and lanthanides elements such as Cm(III) (Brandt et al., 2007), Eu(III) (Finck et al., 2008)
177 and Am(III) (Finck et al., 2015) can also replace part of Mg²⁺ in the octahedral sheet. However, a
178 study from Thien et al. (2010) suggested that Cd²⁺ and Pb²⁺ cannot enter octahedral sheets,
179 because the ions are too large to be accommodated within the magnesium-lithium silicate layer.

180 For the hydrothermal synthesis of hectorite, heating the reactor to 373K-453K is required. At
181 high temperature, well-crystallized hectorite can form in a short time, typically 2h at 473K
182 (Iwasaki, 1989). The reaction time affects the crystallinity and the particle size of hectorite
183 product. The lattice structure of synthetic hectorite is most possibly grown on the verge of the
184 amorphous reactants. With increasing aging time, the crystallinity of hectorite then increases
185 (Carrado et al., 2015). When less crystallization time (4h) is used, the resultant hectorite has

186 smaller particle size and exhibits narrow size distribution with poor crystallinity (Vicente et al.,
187 2009). Hectorite has better crystallinity with larger particle size and higher thermal stability when
188 the crystallization time is long enough (usually, several days)(Sánchez et al., 2013b). Decarreau et
189 al. (2012) revealed that a chemical steady-state (SiO_2 , Na_2O , MgCl_2 as starting gel with LiCl) was
190 reached after 4 weeks at 423K and after 2 months at 443K and 463K. For shorter time (some days
191 at 453K), the 2-dimensional growth of synthetic hectorite along its (001) plane was preferred. In
192 this way, the CEC and the aspect ratio of the synthetic hectorite were then increased (Hai et al.,
193 2018a). Therefore, the temperature and the time for the hydrothermal synthesis of hectorite should
194 be optimized according to the desired features of the products.

195 Commonly, the hydrothermal reaction to produce hectorite occurs at pH 9-10 (Carrado, 2000).
196 When pH value is higher than 11, much OH^- and the enhanced ionic strength may change the
197 nature of precursor gel. In particular, the precipitation and crystallization of $\text{Mg}(\text{OH})_2$ does not
198 occur. If pH is too low, $\text{Mg}(\text{OH})_2$ is dissolved (Sánchez et al., 2013b). In both cases, there is no
199 $\text{Mg}(\text{OH})_2$ as the precursor of the octahedral sheet of hectorite. It is worth noting that hectorite
200 could also be formed from stevensite after Li^+ migration into the vacant site upon dry heating
201 (Petit et al, 2008). More recently, studies show that 2D hectorite-like layers can be scrolled to
202 some degree to form nanotubes under hydrothermal conditions (Hai et al., 2018). Such nanotubes
203 have large outer diameters in the range 100–200 nm and lengths of several micrometers.

204 **2.1.3. Intensified processes**

205 Conventional hydrothermal synthesis of hectorite is conducted at high temperatures for long
206 aging time. It is time-consuming and energy-intensive. Hence, in this context, a rapid process is
207 desired. Microwave heating and ultrasound technology have been used for intensifying the
208 synthesis of hectorite. Microwave oven acts as heater in the hydrothermal synthesis of hectorite.
209 Microwave can provide fast and homogeneous heating and increase the movement rate of reactant
210 molecules. As a result, the crystallization time of synthetic materials is significantly reduced
211 (Vicente et al., 2009). Besides, microwave treatment leads to aggregation with the edge-to-face
212 connections of hectorite nanoparticles, forming a stable structure with mesoporosity (Vicente et al.,

213 2010; Sánchez et al., 2013b). This mesoporous hectorite shows narrow pore size distribution and
214 is more resistant to dehydroxylation than corresponding microporous hectorite.

215 Ultrasonic wave can be used to intensify the mixing of reactants and thus can create more
216 homogeneous mixture of starting materials or precursors of hectorite (Sánchez et al., 2013b).
217 Accordingly, the resultant synthetic hectorite, possesses fewer vacancies in the lattice, lower
218 surface areas and better constructed layers, compared with the synthetic hectorite made by
219 conventional hydrothermal synthesis. For instance, a better incorporation of magnesium and
220 lithium in the octahedral sheet has been achieved by the ultrasound-assisted synthesis (Sánchez et
221 al., 2013a).

222 **2.1.4. Structure-directed synthesis**

223 Organic moieties can be covalently introduced into hectorite by using an organosilane as a
224 silica source $[\text{RSi}(\text{OR}')_3]$, where R stands for alkyl groups and R' for methoxy or ethoxy groups].
225 The method is called *in-situ* synthesis of organo-hectorite and is different from post-grafting of
226 hectorite with organic groups. The silicon atoms of the tetrahedral sheets are covalently bounded
227 to the organic groups present in the interlayer space (**Fig. 4a**). For example, tetraalkoxysilane and
228 organo-trialkoxysilane have been used as the silicon sources. After crystallization under
229 hydrothermal conditions, the moieties of organosilane are covalently attached to $-\text{O}-\text{Si}-\text{O}-$ in the
230 interlayer surface of hectorite (Whilton et al., 1998; Carrado et al., 2001). When the organosilane
231 is used, the crystallization rate of hectorite by *in-situ* synthesis is approximately twice as much as
232 the one when SiO_2 is used (Carrado et al., 2002). This is because the inorganic silica gel usually
233 needs longer time to dissolve and form sol as the silicate precursor species. By contrast, that the
234 silica sol immediately available when a silane is used.

235 Besides acting as blocks in synthetic hectorite, organic species, for example alkyl
236 imidazolium cations, can also act as structure-directing agents or templates (**Fig. 4b**). As a whole,
237 the addition of structure-directing agents into the mixture of reactants aim at producing micro- to
238 mesoporous hectorite (Joshi et al., 2011). The pore diameters depend on the size of organic cation
239 and the amount in the mixture for the hydrothermal reaction. Dependent upon the concentration in
240 water, organic cations can self-assemble and then form different structured supramolecules which

241 act as template. Typically, for such structure-directed synthesis, the alkyl chain length has the
242 effect on the specific surface area, pore size and pore volume of the resultant hectorite. For
243 example, mesoporous hectorites have been synthesized by hydrothermal crystallization of gels
244 containing silica, magnesium hydroxide, lithium fluoride, and 1-butyl-3-methylimidazolium
245 bromide (BMI), 1,3-didecyl-2-methylimidazolium chloride (DDMI) or
246 1-decyl-3-methylimidazolium chloride (DMI) as structure-directing agents at 723K for 48 h
247 (Pawar et al., 2009; Joshi et al., 2011). After calcination, the organic species were burnt and
248 removed and an inorganic porous hectorite with a narrow pore size distribution in the mesoporous
249 range of 3.4 to 5.5 nm was achieved. The pore diameters were found dependent on the molecular
250 mass and size of the imidazolium cations and, to some extent, on its amount used.
251 Tetraphenylphosphonium bromide was also employed as template for producing porous synthetic
252 hectorite (Sethia et al., 2014). The porous hectorite has the single point adsorption total pore
253 volumes of 0.33 cm³/g and a specific surface area of 384 m²/g. Besides, structure-directing
254 synthesis is used to produce hectorite with large nanolayers and good dispersibility in organic
255 solvent (Carrado et al., 1997).

256

257

Fig.4.

258

259 Generally, mild conditions are required to ensure the structural integrity of organic moieties
260 when the structure-directing synthesis and the *in-situ* synthesis is conducted (Carrado, 2000). By
261 contrast, a hard template can endure heating which are usually needed for hydrothermal reactions.
262 Specifically, by using carbon spheres as hard template, hollow microspheric hectorite has been
263 synthesized as demonstrated by Sawant et al. (2014). The carbon spheres were introduced to
264 reaction system by coating with Mg(OH)₂. The synthetic, hollow and microspheric hectorite was
265 obtained by the calcination of hectorite-coated carbon spheres at 773K for 2h at the heating rate of
266 1K/min. The morphology and surface area of hollow and microspheric hectorite can be controlled
267 by the amount and size of carbon spheres. In this way, hierarchically hectorite-based materials
268 have been achieved. Such hard-template synthesis methodology opens new avenues to make many
269 kinds of advanced hectorite-based materials with distinct properties and applications.

270 **2.2 Melt synthesis**

271 A recent study from Christidis et al. (2018) discovered that hectorite products by a
272 hydrothermal process contain up to 25% non-swelling kerolite layers and stevensite, and should be
273 characterized as mixed layer phases. In addition, it has been found long ago that for a
274 hydrothermally prepared hectorite, the charge density is rather heterogeneous and the
275 intracrystalline reactivity is non-uniform (Decarreau et al., 1992). This non-uniformity might
276 result from the solid solution capability of the 2:1 layered silicate structure of hectorite at low
277 temperatures(373-523K) (Muller et al., 1997; Josef et al., 2001). Several studies indicated that
278 melt synthesis, a solid state reaction which the temperature exceeding 1000 K, can provide a
279 solution to the problems and is conducive to producing pure hectorite product with homogeneous
280 charge density (Kalo et al., 2012a; Kalo et al., 2012b; Stöter et al., 2013; Christidis et al., 2018).

281 Josef and his co-workers (2001) demonstrated a melt synthesis of fluorohectorite in gas-tight
282 molybdenum crucibles. The reactants, including SiO₂, MgO and three kinds of fluorides (LiF,
283 MgF₂, NaF), were mechanically rotated during synthesis to assure continuous mixing of the melt
284 at 1823-2373K. However, the cost of the non-reusable crucibles, the limitations of productivity in
285 batch sizes, and the necessity of using highly pure anhydrous chemicals are problematic. Later,
286 Josef's group developed large scale melt synthesis which undergoes at 1538K under argon flow in
287 an open crucible to produce Na⁺-fluorohectorite with superb charge homogeneity and particle size
288 (Kalo et al., 2010). In order to maintain a low vapor pressure of volatile fluorides and sustain a
289 low silica activity, a glass (Na₂O–Li₂O–SiO₂) precursor was used as a fluxing agent. The fluxing
290 agent can inhibit the formation of silicon fluoride gases and promotes the lithium fluoride
291 solubility in the melt. That is why the product showed a superb homogeneity of the charge density,
292 even though this open system leads to unavoidable gradients in composition.

293 In addition, melt synthesis can lead to ordered stacking products. The details of crystal
294 structures for both the one-layer and the two-layer hydrates of hectorite have been uncovered by
295 using the samples from melt synthesis (Kalo et al., 2012a). The cations in the interlayer space of
296 hectorite are located off the central plane and exist in a nine-fold coordination. Namely, a cation
297 coordinated with six basal oxygen atoms and three water molecules. The stacking order of the

298 adjacent 2:1 layer is determined by hydrogen bonding of the water molecules to another
299 tetrahedral sheet.

300 Furthermore, through melt synthesis, synthetic hectorite with very large aspect ratios (>
301 10,000) can be obtained. Kalo et al. (2012b) reported the synthesis of lithium–fluorhectorite at
302 1623K with silicic acid hydrate, MgF_2 and excess $Li_2O-2SiO_2$ glass. This melt-synthesis yielded
303 Li-hectorite has variable layer charge, particle diameter and reactivity increased concomitantly
304 with increasing layer charge. Besides, Stöter et al. (2013) found that long-term annealing can
305 produce Na^+ -fluorhectorite with improved swelling property. The Na^+ -fluorhectorite can
306 delaminate into nanolayers of 1 nm in thickness with an aspect ratio of 18 000.

307 In the melt synthesis hectorite, Li might be introduced to both octahedral and interlayer sites.
308 "In a recent study, Christidis et al (2018) suggested that subsequent annealing of the melt-derived
309 fluorinated hectorite can cause migration of the exchangeable Li into the vacancy of octahedral
310 sheets due to the Hofmann-Klemen effect (Hofmann and Klemen, 1950). As these Li^+ directly
311 balanced the negative charges in the layer, the overall layer charge is decreased and the amount
312 interlayer cations become less (Christidis et al., 2018).

313 **3 Modification**

314 Hectorite possesses several kinds of active sites: the interlayer sites, surface sites, edge sites
315 and inter-particle sites (**Fig. 5**). These active sites can react or interact with other components and
316 hence can be tactically used to modify hectorite. The modification can be conducted by acid
317 treatment, ion exchange, intercalation, grafting and pillaring (**Table 2**).

318 Acid treatment inherently leads to the controlled, ion exchange, partial dissolution or
319 breakage of hectorite because the hectorite attacked by acid and the products are called
320 acid-activated hectorite. The mild acid treatment of hectorite yields a protonated hectorite (Tkáč,
321 1994; Breen and Komadel, 1995). If the acid is strong enough the proton severely attacks the
322 oxygen sites, which connecting the octahedral and tetrahedral sheets on the edge of the faces
323 (Bickmore et al., 2001;Komadel, 2016) and partly damage the structure of hectorite.
324 Consequently, the surface acidity, specific surface area and average pore volume of the
325 acid-activated hectorite are increased (Franco et al., 2016). Typically, such acid-activated hectorite

326 as a catalyst exhibit remarkable acid catalytic activity (Komadel et al., 1997). Acid treatment can
327 also act as a pretreatment of hectorite for further modification.

328 Organic or inorganic cations as exchangeable cations partly or completely replace
329 exchangeable cations in interlayer space of hectorite. In this way, guest cations can be intercalated
330 into in interlayer space of hectorite. When bulky inorganic ions can be intercalated into in
331 interlayer space of hectorite, after calcination the hybrids can be converted into pillared hectorite.
332 Macromolecules can also be inserted into the interlayer space of hectorite to form the intercalated
333 composites (Kotal and Bhowmick, 2015). Besides, the silanol and M-OH groups on the edge of
334 hectorite can react with functional reactive groups of some organic reagents and form a class of
335 grafted hectorite hybrids. Of these modification methods, ion exchange and grafting are more
336 extensively used over the past few decades.

337

338 **Fig.5.**

339

340 **Table 2**

341

342 **3.1. Ion exchange and intercalation**

343 The negative charge on the layer of hectorite is compensated by cations, usually Na^+ and/or
344 Li^+ , in the interlayer space of hectorite. The electrostatically attracted cations can be replaced by
345 other cations by an exchange reaction. Both organic and inorganic cations can be properly selected
346 as the exchangeable cations to partly or completely replace the original exchangeable cations of
347 hectorite.

348 A kind of mixed-cation heterostructures of synthetic Na^+ -fluorohectorite with an K^+ in one
349 interlayer space and Na^+ in one interlayer space in an alternating interstratification pattern can be
350 obtained by the partial cation-exchange reaction between synthetic Na^+ -fluorohectorite and K^+
351 (Möller et al., 2010). The largely different hydration enthalpies (Na^+ by K^+) led to the regular
352 interstratification of hydrated ($d = 12.4 \text{ \AA}$) and nonhydrated ($d = 10.0 \text{ \AA}$) interlayers at 40%
353 relative humidity(**Fig. 6**). Consequently, the original homogeneous charge density in the

354 interlayers of synthetic Na⁺-fluorohectorite was changed. The interlayer space with K⁺ and the
355 CEC of the collapsed nonhydrated (K⁺) interlayers proved to higher and the corresponding
356 hydrated (K⁺) interlayers become lower. This made the interlayers differentiated, allowing it to be
357 selectively manipulated for fabricating bifunctional materials (Stöter et al., 2014;Stöter et al.,
358 2015).

359

360

Fig.6.

361

362 Especially, the ordered heterostructure offers predetermined slippage planes, which can be
363 easily cleaved or exfoliated (Walther and Müller, 2013). For example, after NH₄⁺ exchange of
364 Na⁺-hectorite, ordered heterostructure with alternating NH₄⁺ non-hydrated interlayers and adjacent
365 readily hydrated Na⁺ interlayers are formed (Stöter et al., 2016). Such heterostructural hectorite
366 can be converted into Janus nanoparticles (**Fig.7**). Through osmotic swelling and deprotonation,
367 the bilayers can convert into Janus-type nanoparticles. Similarly, by controlled partial ion
368 exchange, Na⁺-hectorite can also converted into a one-dimensionally (1D)-ordered, regularly
369 interstratified heterostructure with alternating Na⁺ and n-butylammonium (C4) interlayers (Daab
370 et al., 2017). This heterostructure spontaneously delaminates uniformly into single layers upon
371 being dispersed in water to form Janus nanoparticles.

372 Besides inorganic ions, organic cations can also be incorporated into the interlayer space of
373 hectorite through an ion-exchange reaction. Organic cations, such as tallow-triethanol-ammonium
374 (Awad et al., 2009), methyl trioctyl ammonium (Yu and Cebe, 2009), dimethyl dehydrogenated
375 tallow ammonium (Velasco et al., 2007), trimethyl octadecyl ammonium (Dykes et al., 2010) have
376 been used to modify hectorite. Typically, tetramethylammonium chloride (TMAC) dissociates into
377 TMA⁺ cations and Cl⁻ anions in aqueous medium. TMA⁺ cations replace Na⁺ in the interlayer
378 space of hectorite (**Fig. 7a**) (Tan et al., 2014) to form TMA-hectorite. The organic-modified
379 hectorite usually has improved organophilic and hydrophobic. It can delaminate to form
380 monodispersed nanoparticles and organogel in an organic solvent (Wang et al., 2009). Depending
381 on the type of the organic cations, and the packing density and chain length, the corresponding
382 organo-hectorite exhibits different structure and properties (Hendrik et al., 2007). Small

383 organo-ammonium cations, such as tetraethylammonium (TEA^+) do not pack densely and generate
384 empty nanospace in the interlayer space of hectorite due to the local charge repulsion and the
385 stoichiometric balance of the charge (**Fig.7c**) (Bracco et al., 2008). The methylene and methyl
386 hydrogens of TEA^+ interacted with silicon of hectorite. It is well documented that the chain length
387 of organic cations significantly plays a role in the expansion of the interlayer spacing of
388 organohectorite. Compared with the TEA-hectorite, Hectorite intercalated with
389 octadecylammonium ions (ODA-hectorite) has larger interlayer spacing (**Fig. 7f**). Nevertheless,
390 long alkyl chains could completely occupy the interlayer space of hectorite, thereby preventing
391 porosity (**Fig. 7d and e**). In addition, the amount of organo species introduced into the interlayer
392 space of hectorite are crucial to the arrangement of organo cations and then to the porosity. For
393 example, upon the amount of MV^{2+} , MV^{2+} -hectorite (MV^{2+} : 1,1'-dimethyl-4,4'-bipyridinium) has
394 a pore volume of 0.055-0.088 cm^3/g and an average pore size of 0.70-1.43 nm (Okada, 2010).

395 The conventional process to produce organohectorite is relatively costly and tedious because
396 it involves multistep treatments (Yu et al., 2014). Typically, hectorite is dispersed in water and the
397 organic compounds are dissolved in water. Then the two are mixed for an ion exchange reaction so
398 that and quaternary ammonium cations were gradually intercalated into the interlayer space of
399 hectorite. After reaction, the resultant solid need be separated, washed with water and dried upon
400 heating. Such a tedious process is energy-intensive. Moreover, it leads to a large amount of
401 wastewater with excess inorganic ions (e.g. Na^+ , Li^+ , Br^- , Cl^-) and organic cations in it. Therefore,
402 development of a simple and clean process to produce organohectorite is much necessary in
403 practice. Ion exchange reaction between the interlayer cations of hectorite with various
404 phosphonium and ammonium cations have been successfully carried out in supercritical CO_2
405 (Naveau et al., 2009). After reaction and CO_2 evacuation, the organo-hectorite can be directly
406 recovered as a fine powder. Besides, the phosphonium-hectorite is found to be more thermally
407 stable than the conventional alkylammonium- hectorite.

408
409
410

Fig. 7.

411 3.2. Pillaring

412 Pillaring describes a process of transforming a layered compound into a thermally stable
413 micro- and/or mesoporous material with the formation of pillars and the retention of the layer
414 structure (Tsapatsis and Maheshwari, 2008). Pillared hectorite is usually obtained by exchanging
415 the interlayer cations of hectorite with polymeric or oligomeric hydroxymetal cations, followed by
416 converting the hydroxymetal cations into stable oxide pillars in the interlayer space of hectorite
417 upon calcination. The resultant pillared hectorite is micro- and/or mesoporous and thermally stable
418 to some extent (Storaro et al., 1996). Obviously, such pillars can tune the pore size. Pillared
419 hectorite can possess a two-dimensional long range order of pillars and then exhibits a narrow
420 pore size distribution. To achieve this, the hectorite and the pillaring process must be well
421 controlled (Guerra et al., 2008). In addition, Pillars, as building blocks of pillared hectorite,
422 provide additional inner surface and chemical functionality. Hence, selecting pillaring agents and
423 creating different pillars are essential to the physical and chemical properties of the pillared
424 hectorite (Okada and Ogawa, 2003). For example, FeO_x-pillared hectorite was successfully
425 synthesized by intercalation of iron precursors (FeCl₃), followed by calcinations at 573K
426 (Trikitiwong et al., 2014). The surface area was increased from 57.11 m²/g for hectorite to 122.30
427 m²/g for FeO_x-pillared hectorite. Besides, both weak acid sites and strong acid sites were
428 remarkably increased.

429 Generally, the organic pillars bridge the interlayer space in a defined way by penetrating into
430 the hollows on the corrugated silicate surfaces on both sides of the interlayer space. In this way,
431 the hexagonal cavities are forced to be arranged on the opposite each other. But this is not a
432 general law. For example, it has been reported that when large organic pillars, such as
433 1,4-diazabicyclo[2.2.2]octane (DABCO) molecules, were made, the stacking order of the host
434 Cs⁺-hectorite was still preserved and the resultant microporous material does not suffer from
435 stacking faults (Stocker et al., 2008). Besides, when the layer charge of K⁺- hectorite was reduced
436 to x<0.48 per formula unit (pfu) by utilizing the Hofmann-Klemen effect, the pillared hectorite
437 show a significant increase in both micropore volume and pore width (Hofmann and Klemen,
438 1950; Herling et al., 2012) (**Fig. 8a and 8b**). By pillaring K⁺-hectorite with

439 N,N-dimethyl-1,4-diazabicyclo[2.2.2]octane dication ($\text{Me}_2\text{DABCO}^{2+}$), the pore volume ($<10 \text{ \AA}$)
440 of Me_2DABCO -hectorite increases to $0.150 \text{ cm}^3/\text{g}$ from $0.077 \text{ cm}^3/\text{g}$ of K^+ -hectorite (Herling et
441 al., 2012). By contrast, by pillaring K^+ -hectorite with rhodium-tris-2,2-bipyridin trication
442 ($\text{Rh}(\text{bpy})_3^{3+}$), the pore volume of $\text{Rh}(\text{bpy})_3$ -hectorite can be increased to $0.164 \text{ cm}^3/\text{g}$ from 0.112
443 cm^3/g of K^+ -hectorite. The spherical shape of $\text{Rh}(\text{bpy})_3^{3+}$ can create a larger interlayer spacing and
444 the higher charge of $\text{Rh}(\text{bpy})_3^{3+}$ as the pillar make the pillared hectorite need fewer, d more pillars
445 separated from each other, thereby further creating larger available space (**Fig. 8c**). Clearly, the
446 shape and size of the pores of pillared hectorite are not only determined by the layer charge of the
447 hectorite, but also depended on the charge, size, and shape of the pillars.

448

449

Fig. 8.

450

451 **3.3. Grafting**

452 Hectorite has reactive hydroxyl groups on the edges in the form of Si-OH and $\text{Mg}(\text{Li})\text{-OH}$
453 groups, and inside the layer in the form of Mg-OH or Li-OH groups. In particular, the reactive
454 silanol groups are readily accessible to functional groups of organic agents. It is now also found
455 that the high negative charge of hectorite (approximately 700 electron charges pfu) effectively
456 facilitates the nuclear substitution reaction in which hectorite reacts with alkylsilane to generate
457 new O-Si bonds, as called a grafting process by silylation (Delavernhe et al., 2018). Such
458 silylation of hectorite allows the formation of $-\text{Si-O-R-O-Si}-$ linkages between hectorite
459 nanoparticles (Daniel et al., 2008).

460 The grafting between hectorite and hydrophobic silane groups takes place mainly on the
461 external surface, while the interlayer space remains nearly intact (Yang et al., 2013; González et
462 al., 2017). When the silylating agent was grafted on the edges of the hectorite layers, the
463 individual hectorite nanolayers was chemically locked into irreversibly stacks (Norma et al., 2004).
464 Recently, Yang et al. (2013) successfully fabricated amphiphilic hectorite with hydrophobic edge
465 and hydrophilic face, which had distinct surface activity and wettability. The process involved two
466 steps, hydrolysis and polymerization (**Fig. 9**). Firstly, the silanols of the hectorite reacted with

467 siloxy groups of dimethylethoxysilane (DMES), hence grafting of Si–H onto the edge of hectorite
468 nanoparticles. Secondly, through the reaction between new created Si–H bond on the edge of
469 grafted-hectorite and 1-octadecene, the hydrophobic alkane chains then grafted successfully onto
470 the hectorite nanoparticle.

471

472

Fig.9.

473

474 Some organic species also can be grafted on both the external surface and internal surface of
475 hectorite. The basal spacing of 2-(3-(2-aminoethylthio) propylthio)ethanamine (AEPE) modified
476 hectorite increased to 18.4 Å from 12.7 Å of hectorite (Phothitontimongkol et al., 2009). A large *d*
477 spacing of 20.1 Å was also observed after the intercalation and grafting of
478 (3-aminopropyl)-triethoxysilane to hectorite. The grafting process consists of the condensation of
479 ethoxy groups of (3-aminopropyl)-triethoxysilane on the surface of hectorite. With the presence of
480 thioether group in the ligand, the van der Waals interaction among ligand chains may occur,
481 leading to its structural rearrangement and the contraction of the interlayer spacing of hectorite.

482 Grafting significantly changes the physical and chemical properties of hectorite surface
483 (Guerra et al., 2009). By a condensation reaction of the hectorite edge silanol groups with different
484 silylating agent, different covalently-functionalized hectorite nanoparticles can be obtained. For
485 example, the basal spacing and surface area of hectorite are increased when trialkoxy silanes are
486 used (Wheeler et al., 2005), while flat monolayer on the edge of the hectorite plates, and only
487 minimal effect on the basal spacing and surface area are observed when monoalkoxy silanes are
488 used (Phothitontimongkol et al., 2013). But because of their smaller particle size, monoalkoxy
489 silane-hectorite exhibit generally better dispersion than other large alkoxy silanes-hectorite.

490 In addition, the texture and properties of the surface functional groups on the grafted hectorite
491 strongly depend on the grafting route. For example, hectorite-aminosilane hybrid materials have
492 been prepared by a reaction of hectorite with amino silanes. The aminosilane are made from a
493 reaction of (3-chloropropyl) triethoxysilane (CIPTES) with biuret and melamine in toluene and
494 then to it hectorite added for grafting (González et al., 2017). Alternatively, CIPTES were slowly
495 added to the hectorite dispersion and then biuret and melamine was added and the hydrolysis was

496 catalyzed by HCl acid. The toluene non-aqueous condition and the aqueous acidic condition
497 lead to physico-chemical and adsorptive properties of the hybrids. .Due to acid-catalyzed
498 hydrolysis of the alkoxide, the hybrid made under aqueous acidic condition possessed higher
499 specific surface area.

500 Due to the distinct ratio of edge to surface of 0.07 (Delavernhe et al., 2018), hectorite is used
501 as an ideal material for studying combined edge and surface modification. Dual modification of
502 hectorite refers to simultaneous surface modification and edge modification. In an earlier study,
503 dual-functional hectorite was synthesized by a condensation reaction with silane coupling agents
504 and a cation exchange reaction with quaternary ammonium cations (Wang et al., 2007). In this
505 way, quaternary ammonium chains can be grafted to hectorite edges, creating star-like or fringed
506 products with a nanosized inorganic core. In another study, double-chain surfactant
507 dimethyldioctadecylammonium cation was employed as cation exchanger and
508 3-(trimethoxysilyl)propyl methacrylate was employed as an edge covalent modifier (Borsacchi et
509 al., 2007). After such modification, the adjacent hectorite nanoparticles were twisted, resulting in
510 an increased disorder in the hectorite nanoparticles. Mishra et al. (2011) prepared two types of
511 dual modified hectorite. One was hectorite modified by cetyl trimethyl ammonium cations
512 followed by silylation with octyl trimethoxy silane; the other was hectorite modified by cetyl
513 trimethyl ammonium cations followed by silylation with 3-aminopropyl triethoxy silane (**Fig.10**).
514 Then after the dual modified hectorite reacted with the hard segments of thermoplastic
515 polyurethane (TPU), the resultant nanocomposites exhibited different aggregated morphologies
516 (tubular, elliptical and spherical), thus resulting in the difference in segmental relaxation, and
517 mechanical and rheological properties of the nanocomposites.

518

519

Fig.10.

520

521 **4 Assembly**

522 **4.1. Layer-by-layer assembly**

523 Layer-by-layer (LBL) assembly is a process to produce multilayered films from lamellar
524 material by repeated assembly of one layer over the other layer. It can be conducted on polymer
525 surface (Wagner, 2007). LBL assembly can be driven by electrostatic forces (Such et al., 2006),
526 covalent bonds (Buck et al., 2007) or hydrogen bonding (Gao et al., 2018). Hectorite can be easily
527 dispersed and exfoliated in water to form individual nanolayers, and by LBL technique, the
528 nanolayers can be used to produce homogeneous and continuous hybrid film (Fenero et al., 2017).

529 Hectorite nanoparticles can be deposited in a LBL way and assembled on polyvinyl alcohol
530 (PVA) surface to form films through hydrogen bonding and adsorption (Patro and Wagner, 2011).
531 The LBL films exhibit better mechanical properties than pure PVA, mainly because hectorite
532 nanoparticles being oriented, leading to efficient interfacial stress transfer. In addition, the
533 overlapping dispersed hectorite nanolayers can act as individual barriers to gas infiltration and
534 created a more tortuous and longer path for gas molecules moving through the polymer matrix
535 (Keeling et al., 2012). Thus the transport of molecules, atoms and ions in the film can be tuned. A
536 recent study (Patro and Wagner, 2016) revealed that graphene oxide (GO) can be dispersed in
537 aqueous hectorite dispersion and the two nanolayers can be used for layer-by-layer assembly. In
538 this way, GO was easily incorporated into polyvinyl alcohol (PVA)/hectorite LBL films. The LBL
539 films appear to be uniform and the thickness of the layer increased linearly with the number of
540 depositions.

541 By LBL assembly, hectorite nanolayers can be used for making multilayer reverse osmosis
542 membranes. Generally, the multilayer reverse osmosis membrane shows excellent rejection
543 capability, wide pH tolerance, low permeability and poor chlorine stability (Priolo et al., 2013; Liu
544 et al., 2014b; Cho et al., 2015). The combination of the nanochannels in the interlayer of hectorite
545 and the high porosity of the nanofiber mat support high separation efficiency with simultaneously
546 high permeability of thin film nanocomposite nanofiber membrane. Rajeshwe et al. (2017)
547 incorporated hectorite nanoparticles into the layers formed between trimesoyl chloride (TMC) and

548 m-phenylenediamine (MPD). Hectorite nanoparticles were physically attached with the amide
549 linkages through hydrogen bonding to form the trilayer structure. The incorporation of hectorite
550 facilitated rapid growth of the selective layer, 29 nm per layer for the trilayered
551 TMC/MPD/hectorite, compared with 9 nm per layer of the bilayered TMC/MPD.

552 LBL assembly can also applied to make hectorite nanohybrids. For example, by LBL
553 assembly Xiao et al. (2016) prepared polyelectrolyte multilayer-coated doxorubicin
554 (DOX)/hectorite nanohybrids. DOX was firstly loaded onto the surface of hectorite via
555 electrostatic interaction. Then DOX-loaded hectorite was alternatively coated with positively
556 charged poly(allylamine) hydrochloride (PAH) and negatively charged poly(sodium styrene)
557 sulfonate (PSS). The nanohybrids can be used as novel DOX delivery systems with sustainable
558 and controllable drug release. Recently, a kind of nitrogen-doped carbon nanodot
559 (NCND)-hectorite hybrids was obtained by LBL assembly (Dimos et al., 2017). The NCND had
560 excellent solubility in water and abundant nitrogen-and oxygen-bearing functional groups on their
561 surface. Hence, such small fluorescent NCND can be intercalated into the interlayer space of
562 hectorite by an ion-exchange reaction. Firstly, dimethyldioctadecylammonium (DODA)-hectorite
563 monolayer was prepared at the air/water interface and attached onto a substrate. Then the
564 DODA-hectorite layer was dipped into a solution of NCND for self-assembly, resulting in a
565 luminescent DODA-hectorite-NCND multilayer film (**Fig. 11**). Moreover, the inert hectorite
566 nanoparticles not only guide the highly ordered 2D assembly of NCND in the interlayer space of
567 hectorite but also protect them from external agents.

568 **Fig.11.**

569

570 **4.2. Templated assembly**

571 Hectorite nanoparticles can be assembled in a structure-oriented way with the aid of a
572 template. Such templated assembly method can combine with LBL assembly and such
573 methodology can be used to fabricate nano- or microcapsules with hectorite in the structure. For
574 example, by using Pickering emulsion template and electrostatic LBL self-assembly, Liu et al.
575 (2014a) successfully prepared nanocomposite polysaccharide microcapsules composed of

576 biocompatible polyelectrolyte complexes. The LBL deposition occurred between sodium alginate
577 (ALG) and chitosan (CS) on Pickering emulsion droplets. They were stabilized by
578 poly(ethyleneimine) (PEI) -modified hectorite nanoparticles. Hollow multilayer microcapsules are
579 obtained after removing the core by washing with 2-propanol (**Fig. 12**). These hollow
580 microcapsules are well-dispersed in organic solvent and show long-term stability for more than
581 two months. In addition, the size of the microcapsules can be tuned (from several to tens of
582 micrometers) by altering the mass ratio of PEI/hectorite.

583

584

Fig.12.

585

586 By a templated self-assembly process, a water-dispersible multifunctional
587 polyaniline-hectorite-keggin iron nanotube has been achieved (Sudha et al., 2011). The negative
588 ions on the surface and residual positive charges on the edges of the hectorite disc adsorbed both
589 keggin iron and aniline through ion-dipole and ionic interactions. That is to say, hectorite can act
590 as a micellar template during polymerisation. During polymerization, the disorganized keggin
591 iron-hectorite nanoparticles were co-structured, and then self-assembled with the polyaniline and
592 the engulfed layers and rolled sheets of nanotubes. The multifunctional
593 polyaniline-Laponite-keggin iron nanotubes exhibited electrical conductivity, saturation
594 magnetization and thermal stability (573K). More recently, Huang et al. (2018) demonstrated a
595 co-assembly method for making ordered inverse opal-like porous hectorite films with well-defined
596 pore size that are crack-free over a large area (on the scale of cm^2). Hectorite nanolayers were
597 co-assembled with polystyrene latex nanoparticles into colloidal crystals. The polystyrene latex
598 were used as a sacrificial template, which was burnt by calcination (**Fig. 13**). The change of the
599 ratio of hectorite to polystyrene changes in the quality of film. The hygroscopic nature of the
600 hectorite can slow the film drying and therefore mitigate cracking. Another possible reason was
601 that the stacking and overlap of hectorite nanolayers distributed evenly the stress, thereby reducing
602 cracking.

603

604

Fig. 13.

605

606 Janus nanoparticles are a type of nanomaterials with asymmetric structure, Namely, the two
607 sides of a Janus nanoparticle are different in composition or polarity. The exchanging ions will
608 change the surface charge potential of hectorite, depending on the type of ions exchanged. A
609 hectorite nanoparticle has anisotropic surface potentials on either side and thus it can be made into
610 Janus particles. For example, Janus colloids composed of hectorite-armed poly(divinylbenzene)
611 can be obtained through a double Pickering emulsion template (Pardhy and Budhlall, 2010).
612 Polystyrene or poly(divinylbenzene) colloids stabilized with hectorite were synthesized first to
613 form hectorite-armed colloids (**Fig. 14a and b**). Then, the nanoparticle-stabilized colloids were
614 templated at a wax-water interface in order to modify one hemisphere of the colloids (**Fig. 14c**).
615 The hectorite nanoparticles on the aqueous side are ion exchanged (Na^+ by Ca^{2+} , Fe^{2+} , and Fe^{3+}) in
616 the dispersion. After breaking Pickering emulsion, Janus colloids were obtained (**Fig. 14d**). The
617 diameter of the polystyrene (PS) particle can be controlled by adjusting the ratio of oil and
618 hectorite. Liu et al. (2013) described the assembly of amphiphilic Janus hectorite nanoparticles by
619 using surface immobilization. The positively charged PS colloidal nanoparticles acted as templates.
620 One side of a hectorite nanoparticle touched the surface of PS colloidal particle, and the other side
621 of hectorite nanoparticle faced the aqueous medium (**Fig. 15**). After redispersing the colloidal PS
622 nanoparticles into tetrahydrofuran (THF)-water mixture, amphiphilic Janus hectorite nanolayers
623 with PS chains on one side and hydrophilic quaternized poly(2-(dimethylamino)ethyl
624 methacrylate(q-PDMAEMA) or polymeric micelles on the other side were obtained.

625

626

Fig. 14.

627

628

Fig. 15.

629

630 **4.3. Hierarchical assembly**

631 Supramolecular self-assembly based on multiple noncovalent forces is an effective way to
632 fabricate multiple stimuli-responsive hydrogel. However, such organic supramolecular

633 nanostructured materials are always subjected to weak mechanical strength. The hierarchical
634 organic-inorganic supramolecular assembly can introduce hectorite into the supramolecular
635 hydrogels and enhance the mechanical properties of supramolecular hydrogels. It also reduces the
636 organic consumption. Supramolecular hydrogel with strong luminescence, extraordinary
637 mechanical property, and self-healing ability were also obtained by hierarchical organic-inorganic
638 self-assembly (Li et al., 2017a; Li et al., 2017b; Li et al., 2018). An organic ligand consisting of a
639 terpyridine unit and two flexibly linked methylimidazole moieties (**Fig. 16a**) acted as emitting
640 sources (Li et al., 2017a). Synergistic coordination of thenoyltrifluoroacetone and terpyridine units
641 led the monomer to self-assemble into spherical micelles in water, thus maintaining the
642 luminescence of Ln complexes in water (**Fig. 16b**). These micelles further co-assemble with
643 sodium polyacrylate (ASAP)-exfoliated hectorite nanolayers into networks (**Fig. 16c**). Association
644 of hectorite nanoparticles coated with oxyanions with the imidazolium salts on the surface of the
645 supramolecular assemblies via electrostatic interactions resulted in formation of robust
646 luminescent hydrogels. Another design proposed the self-supported supramolecular hydrogels can
647 be constructed through the hierarchically assembly of hectorite with cyclodextrin-based
648 pseudopolyrotaxanes (PPRs) (Li et al., 2017b). The cooperative interactions between the
649 PPR-involved guanidinium parts and the negatively charged hectorite nanoparticles played a
650 crucial role in the formation of supramolecular hydrogels. The hydrogels have tunable mechanical
651 strength, which modulated by tuning the molecular weight of polymeric chains in the central
652 pseudopolyrotaxanes. Later, Ln ions and guanidinium-azobenzene (Guazo) units were chose as
653 luminescent emitting ions and photo-switches (Li et al., 2018). The host-guest complexes consist
654 of α -cyclodextrins (α -CDs) and azobenzene (**Fig. 17**). The Ln-containing host-guest complexes
655 subsequently served as binders for the incorporation of exfoliated hectorite into the hydrogels. The
656 hybrid luminescent hydrogels were formed through the construction of multivalent salt bridges
657 involving hydrogen bonding and electrostatic interactions between the guanidinium groups and
658 the oxyanion groups on the surface of the hectorite. These luminescent supramolecular hydrogels
659 showed excellent mechanical strength, color-tunable luminescence, and photoirradiation
660 reversibility.

661

662 **Fig.16.**

664 **Fig.17.**

666 Besides, two types of nanoparticles of clay minerals can be mixed together to be added into
667 hydrogels. Hectorite (aspect ratio of 25) and montmorillonite (aspect ratio of 250) were used to
668 fabricate bicontinuous gels by hierarchical self-assembly (Pujala et al., 2018). The bicontinuous
669 gels exhibited foam-like morphology with pore size of a few micrometers. The pore size in
670 bicontinuous gels can be tuned by varying the g ratio of hectorite/montmorillonite nanoparticles
671 **(Fig. 18).**

673 **Fig. 18.**

674 **5. Applications**

675 Hectorite has been commercially used in such industries as cosmetics, detergents, coatings,
676 and paints in which the excellent colloidal properties of hectorite nanoparticles are advantageous.
677 A small amount of hectorite is added into the polymeric system can form functional hydrogels
678 with improved properties. Hectorite can also be used as adsorbents and catalysts. Recent years has
679 witnessed that hectorite nanoparticles are increasingly studied for being used in analysis, energy
680 materials and biomaterials. For instance, hectorite-coated spherical silica particles were used as
681 chiral high performance liquid chromatography column packing materials (Tomohiko et al., 2018).
682 The layered hectorite nanoparticles can improve optical resolution and reduce the volume of
683 mobile phase used. Yang and Zhang (2018) successfully developed a hectorite nanolayer/carbon
684 black-coated Celgard separator to inhibit polysulfide shuttle of lithium-sulfur (Li-S) battery
685 efficiently. Besides, the abundant Li^+ and the layered nanostructure of the hectorite nanolayer
686 enhanced the Li^+ conductivity. Consequently, the Li-S batteries showed a high initial reversible
687 capacity, high rate performance, superior cycling stability, and ultralow self-discharge.

688 **5.1. Adsorbent**

689 Hectorite has been used as adsorbents for selectively adsorbing heavy metals, gas, dye and
690 organic compounds. The driving force of adsorption involves chemical bonding, electrostatic
691 attraction, Van der Waals force, surface complexation, and ion exchange between adsorbates and
692 the surface of hectorite. In addition to surface reactivity, the adsorption behavior of hectorite is
693 also related to the oxygen defects of the Mg–O octahedra and the Si–O tetrahedra (Bian et al.,
694 2015).

695 Some studies suggested that hectorite has better adsorption selectivity and capacity towards
696 metal ions after being modified with organic ligands-containing metal-chelating groups. For
697 example, 2-(3-(2-aminoethylthio) propylthio) ethanamine (AEPE)-modified hectorite is a good
698 adsorbent for Hg(II) ions with adsorption capacity of 54.7 mg/g in a solution contained 140 mg/l
699 Hg(II) ions at pH 4 (Phothitontimongkol et al., 2009). AEPE-hectorite also showed a good
700 selectivity toward silver ions in the solution pH ranged from 4 to 9 and the maximum adsorption
701 capacity was 49.5 mg /g (Phothitontimongkol et al., 2013). The improvement is ascribed to high
702 affinity of the AEPE ligand for binding Ag(I) ions and Hg(II) ions, preventing the detachment of
703 the metal ions from the surface of hectorite. Similarly, the adsorption capacity of
704 bis[3-(triethoxysilyl)propyl] tetrasulfide-modified hectorite for U(VI) from wastewater (18.99
705 mmol/g) comes from the high affinity for binding silver ions of the ligand (Guerra et al., 2010;
706 Lee and Koo, 2011)

707 Pillared hectorite also has selective adsorption for gas because of the high specific surface,
708 the size and volume of micropores, and of the pillars. Pillared hectorite showed an adsorption
709 selectivity for CO₂ over N₂, and the volume ratio of adsorbed CO₂ to adsorbed N₂ reached 1.9 at
710 303K (Pawar et al., 2009). The mesoporous hectorite based on calcined
711 tetraphenylphosphonium-modified hectorite had a high surface area of 384 m²/g and showed a
712 very good adsorption selectivity for CO₂ over N₂, CO, CH₄ and O₂ (Sethia et al., 2014). The CO₂
713 adsorption capacity for mesoporous hectorite was 22.8 cm³ /g at 288 K. Theoretically, CO₂ has
714 higher quadrupole moments and polarizability than N₂, CO, CH₄ and O₂. The principal interaction
715 of the gas molecules with hectorite came from the electrostatic interaction between lattice oxygen

716 atoms and interlayer Li^+ cations of hectorite, and this electrostatic interaction depends on the
717 quadrupole moments, dipole moment and polarizability of the gas molecules.

718 Dyes in the wastewater cause environmental issues because they are toxic, mutagenic or
719 carcinogenic. Hectorite has been experimentally used as an adsorbent for the removal of cationic
720 dyes. The interaction between hectorite and cationic dyes were divided into two ways, ion
721 exchange (Baskaralingam et al., 2007; Fujimura et al., 2016) and electrostatic interactions
722 (Lezhnina et al., 2012). For example, cetylpyridinium-modified hectorite acted as an effective
723 adsorbent for Neutral Red in aqueous solution and showed an adsorption capacity of 393.70 mg/g
724 (Yue et al., 2011). The adsorption capacity of hectorite for methylene blue (MB) at pH 6.5 was
725 1.162 mmol/g (Hegyési et al., 2017). In this case, the isoelectric point at the edge and the
726 negatively charged basal surface of hectorite were covered by MB^+ cations (Pawar et al., 2018).

727 Hectorite is also used to adsorb organic compounds. Aflatoxin, a kind of toxic and
728 carcinogenic biotoxin, can be adsorbed by hectorite (Bbosa et al., 2013) The diffused octahedral
729 layer charge in hectorite allowed more accessibility to the interlayer space and less repulsion for
730 aflatoxin molecules than other smectites where the charge was of tetrahedral origin. In addition,
731 the size and polarity matching between the adsorbing domains and aflatoxin molecules in the
732 interlayer was influenced by the exchangeable cation (Barrientos-Velázquez et al., 2016).
733 Trimethoprim, 5-(3,4,5-trimethoxybenzyl) pyrimidine-2,4-diamine (TMP), is an antibiotic drug
734 that cannot be completely metabolized by the human being (Ji et al., 2016). When the hectorite
735 was grafted with aminosilane, the presence of well-dispersed active sites favors the adsorption of
736 TMP onto hectorite-aminosilane hybrid materials. The interactions between trimethoprim and
737 hectorite are hydrogen bonding and Lewis acid-base interactions and cation exchange. As a result,
738 the removal percentage for TMP was larger than 80% (González et al., 2017).

739 **5.2. Catalyst**

740 Hectorite have been widely used as a host or a support for metal-based catalysts and
741 oxide-based catalysts. Incorporating the active metals (e.g. Ru, Cu) or oxides into the interlayer
742 space of hectorite allows those active species to be highly dispersed, thus enhancing acid-base or
743 redox catalytic performance. So far the catalytic properties of hectorite have been experimentally

744 evaluated for many catalytic reactions (**Table 3**). Generally, due to the thermal stability of
745 hectorite, the temperatures for the catalytic reactions upon heating are not as high as 873K.

746 Cu can be supported onto delaminated hectorite by impregnation and ion-exchange methods.
747 The Cu/hectorite catalyst has proved catalytically active for the selective glycerol hydrogenolysis
748 to 1,2-propanediol in liquid phase (Sánchez et al., 2012). The conversion of glycerol can reach to
749 61% and the selectivity to 1,2- propanediol was 93% after 8 h of reaction at moderate conditions
750 (40 bar, 473 K). The high surface area and lower hydrophilic character of the delaminated
751 hectorite played a role in avoiding Cu agglomeration. Cu/delaminated hectorite catalyst was also
752 able to accelerate the oxidation of NO to NO₂ (Sánchez et al., 2013a). For a gas mixture of 500
753 ppm NO_x/5% O₂/N₂, over the Cu/hectorite catalysts for 5000s at 873K, the soot conversion can
754 reach 100%. The main role of the Cu/hectorite catalyst was to activate O₂ molecules, thereby
755 facilitating NO to NO₂. Hectorite can also be introduced into the microgel of cationic Pb
756 precursors by ion exchange to obtain Pd-containing ternary microgel nanocomposites. The
757 microgel nanocomposites as catalysts are active for the Suzuki reaction of aryl iodides in
758 water-rich medium under mild condition (353K, 4h). The higher catalytic efficiency was observed
759 in the case of microgels with the higher hectorite content (Contin et al., 2014).

760 Ru nanoparticles can be intercalated in the interlayer space of hectorite to give a black solid
761 catalyst (Süss-Fink et al., 2006). The Ru nanoparticles/hectorite exhibited hexagonal or spherical
762 shapes with the size in the range of 4–38 nm. It was a highly efficient and reusable catalyst in the
763 hydrogenation of benzene (Süss-Fink et al., 2009). Ru/hectorite nanoparticles can catalyze the
764 hydrogenation of benzene to cyclohexane under mild conditions (323K) and the turnover
765 frequencies (TOF) reached up to 6500 catalytic cycles per hour (Süss-Fink et al., 2009).
766 Ru/hectorite nanoparticles (particle size ~ 4nm) were also able to catalyze the hydrogenation of
767 furfuryl alcohol to tetrahydrofurfuryl alcohol in methanolic solution at 313K under a hydrogen
768 pressure of 20 bar (conversion 100%, selectivity>99%) (Khan et al., 2011). After a total turnover
769 number of 1423, Ru/hectorite nanoparticles were deactivated but can be recycled and regenerated.
770 In addition, Ru/hectorite (particle size ~7 nm) was found to catalyze the specific hydrogenation of
771 the C=C bond in α,β -unsaturated ketones (conversion 100%, selectivity > 99.9%) (Khan et al.,
772 2012). The catalytic turnovers range from 765 to 91,800 under mild conditions (temperature 308K

773 and constant hydrogen pressure 1–10 bar). Besides, Ru/hectorite nanoparticles can also catalyze
774 the hydrogenation of quinoline at 373K under 30–60 bar H₂ with solvent-switched selectivity: in
775 water, 1,2,3,4-tetrahydroquinoline was formed with yields >99%, whereas in cyclohexane the
776 fully hydrogenated decahydroquinoline was obtained with yields >99% (Sun et al., 2013).

777 FeO_x-pillared hectorite was a highly effective catalyst for the conversion of epoxides to
778 acetonides (Trikitiwong et al., 2014). The preparation of catalyst mainly involved the
779 intercalation of FeCl₃ into hectorite interlayers and calcination. At 303K for 30min, the conversion
780 of styrene oxide to 2,2-dimethyl-4-phenyl-1,3-dioxolane by different FeO_x-pillared hectorite
781 catalyst in 83% yield. In addition, the catalyst can be recovered and reused up to five times
782 without appreciable loss of activity. More recently, researchers have been discovered that the
783 adsorption of the amino acid on the surface of hectorite led to the increased enantioselectivity in
784 the asymmetric Michael addition (Szöllősi et al., 2018). The heterogeneous chiral catalyst
785 maintained stereo selectivity in the asymmetric addition of aldehydes to nitrostyrenes.

786 A class of thermally stable and mesoporous metal oxide/ hectorite nanoparticles have been
787 earlier studied by Zhu et al (2002, 2006) for the degradation of Rhodamine 6G in aqueous solution.
788 TiO₂/hectorite proved to be a heterogeneous photocatalyst (Hashimoto et al., 2005). In particular,
789 mesoporous TiO₂/hectorite had large mesopores which were beneficial to the diffusion of organic
790 molecules to access to the active sites (Yang et al.,(2010). The use of hectorite could help to form
791 a specific TiO₂ nanoparticles with high photocatalytic activity. Recently, a photocatalytic hybrid
792 film of anatase and hectorite was successfully fabricated by Deepracha et al. (2019). The film was
793 adhered on the glass substrate stably enough for the photocatalytic decomposition of methylene
794 blue and methyl orange in an aqueous acidic solution.

795 Hectorite have also been used for the controlled formation and stabilization of core–shell
796 nanocrystals with enhanced stability and large surface area. This core-shell Pd–Pt-hectorite
797 composites were active catalysts for the reduction of 4-nitrophenol with NaBH₄ in aqueous
798 solution (Varade and Haraguchi, 2014). As a result of the presence of hectorite, the catalysts
799 showed superior resistance to undesirable agglomeration of active sites and thus exhibited the
800 exceptional catalytic activity. Bis(oxazoline)-metal complexes have been used as catalysts in
801 many enantioselective reactions. They can be supported by cationic exchange into hectorite, and

802 that the solids thus obtained are able to promote the benchmark cyclopropanation reaction
803 between styrene and ethyl diazoacetate with the enantio selectivity in the range of 16-20% (Ben
804 Zid et al., 2017).

805

806

Table 3

807

808 5.3. Fluorescent reporter

809 Hectorite can act as a carrier for many organic dye molecules for functionality in optical
810 spectroscopic analysis. Typically, dye/hectorite hybrid nanomaterials combine the optical and
811 spectroscopic properties of organic dyes with the physical and chemical properties of hectorite
812 (Duque-Redondo et al., 2014). The hybrid nanomaterials have a potential for nanoscale
813 fluorescent reporters and optical probes for a variety of fluorescence-based analytical and
814 diagnostic applications (Suzuki et al., 2011; Dawson and Oreffo, 2013; Takagi et al., 2013; Elder
815 et al., 2014; Fujimura et al., 2016).

816 The adsorption of organic fluorophores such as methylene blue (Schoonheydt, 1991),
817 toluidine blue (Yurekli et al., 2005), rhodamine 6G (R6G) (Arbeloa and Martínez, 2011) and
818 crystal violet (Ley et al., 2015b) onto the hectorite surface is mainly driven by electrostatic
819 interactions. Generally, dispersing the dye on the hectorite surface enriches dye population and
820 (Yurekli et al., 2005). Fluorescence polarization is used for evaluating the preferential orientation
821 of fluorescent dyes adsorbed in hectorite layers in a macroscopic scale (Arbeloa and Martínez,
822 2011). For example, R6G monomers were adsorbed onto the hectorite layers as monomeric units
823 for low-loading films, with a preferential orientation of around 62° with respect to the normal of
824 the film. Indeed, the electrostatic interactions between negatively charged basal surface of
825 hectorite nanoparticles and dye molecules can be used to tune the photophysical properties of dye.
826 Ley et al. (2015b) found that the strong electrostatic interaction between hectorite and Crystal
827 Violet cationic molecules hinders phenyl ring movements and consequently inhibited the
828 formation of dark state. As a consequence, light energy was stored in a singlet emissive bright
829 state, turning this nonemissive dye into a fluorescent one. Similarly, the electrostatic interaction of

830 Astrazon orange R (AO-R) on the hectorite nanoparticles prevented the isomerization of the dye
831 after light absorption, stabilizing the emissive singlet excited state of the dye (Tsukamoto et al.,
832 2015; Ley et al., 2015a).

833 Hectorite has been experimentally loaded with perylenes, cyanines, merocyanines, and
834 coumarines (Grabolle et al., 2016). The adsorption of such neutral dyes or zwitterionic dyes onto
835 the hectorite was achieved by van der Waals interactions (Suzuki et al., 2011) and hydrogen
836 bonding (Dawson and Oreffo, 2013). Adsorption of the dyes onto hectorite nanolayers brought
837 about changes in the spectra and intensity of absorption and emission. The intensity was
838 dye-specific, depending on dye charge and character of the optical transitions involved. The
839 fluorescence quantum yields reached at least 0.20 even at the highest dye loading concentration of
840 up to 50 dye molecules per hectorite platelet. This was because hectorite had flat surface at atomic
841 level, positive or negative charges in the structure and optical transparency in a state of aqueous
842 dispersion. Dye molecules on the hectorite surface could change their structure and intramolecular
843 vibrational motion, thus changing their fluorescence properties (Tokieda et al., 2017). This
844 fluorescence enhancement phenomena of dyes on the hectorite surface are named as
845 “Surface-Fixation Induced Emission (S-FIE)”.

846 The loading of hydrophobic dyes onto hectorite makes it accessible in aqueous environments
847 (Gaharwar et al., 2013). Besides, combining different types of organic dyes and hectorite can
848 tailor photoactive properties (Staniford et al., 2015) and the microscopic order of the dye
849 molecules and make them homogeneous dispersed (Hill et al., 2015). For example, employing
850 hectorite as inorganic matrix combined with native aluminium hydroxide phthalocyanine
851 (Al(OH)Pc) led to a novel organic–inorganic hybrid materials (Staniford et al., 2015) (**Fig. 19**).
852 Not only were the solubility and aggregation bottleneck of Al(OH)Pc tackled simultaneously, but
853 also the efficient emission of Al(OH)Pc–nanoclay hybrids and generation of singlet oxygen was
854 achieved in aqueous solution.

855

856

Fig. 19.

857

858 Dye/hectorite hybrid nanomaterials can act as nanoscale fluorescent reporters for
859 fluorescence-based analytical and diagnostic applications. For example, hectorite-Astrazon orange
860 R(AO-R) can form very efficient hybrid photoinitiators. The dye molecules were intercalated in
861 the interlayer space, located at the edges or at the surfaces of the stacked layers. Hence, the
862 photophysics of the AO-R molecules can be adjusted. The conversion rates at a constant resin
863 viscosity were increased by the 4-fold (Ley et al., 2017). Li et al. (2015) demonstrated an
864 organic-inorganic nanohybrid luminescent pH detector by loading a Europium(III) - β -diketonate
865 complex into hectorite. It worked under acid conditions and can serve as highly robust, reliable,
866 rapid responsive and sensitive fluorescent pH detector. Au/hectorite nanoparticles as enhanced
867 substrates can be applied to surface enhanced Raman scattering (SERS) (Hill et al., 2016).
868 Hectorite not only played the role of template during the growth of Au nanoparticles, but also
869 increased dye adsorption, thus achieved the enhanced local electric fields generated by the
870 plasmon, thus improving the SERS sensitivity.

871 In addition, the presence of hectorite nanoparticles in the solution not only influences the
872 optical properties of the dye, but also influences other properties. The aggregation of cationic
873 p-phenylene ethynylenes oligomers (OPE) exhibited strong antimicrobial activity and strong
874 photophysical changes, can thus be utilized for sensing various chemicals and biomolecules (Tang
875 et al., 2011). OPE aggregate on hectorite and induce aggregation of hectorite nanoparticles,
876 leading to drastic changes to their photophysical properties and other properties. Solid
877 OPE-hectorite films were shown to have fair resistance to dissolution in aqueous solution
878 compared with hectorite alone (Hill et al., 2015). Besides, in presence of hectorite, the second
879 harmonic generation (SHG, also called frequency doubling) active J-aggregate of a thiocyanine
880 dye N, N'-dioctadecylthiocyanine perchlorate (TC18) in Langmuir-Blodgett (LB) films exhibited
881 good stability due to the presence of electrostatic force between thiocyanine dye and hectorite
882 (Debnath et al., 2017).

883 **5.4. Hydrogel**

884 Hydrogel is a large water-filled inorganic or organic polymeric network in variable gel form.
885 Hydrogels are mainly formed via physical or chemical crosslinking of inorganic or organic

886 molecules or nanoparticles. Usually, physical hydrogels are unstable while chemical hydrogels are
887 brittle and lacking of self-healing ability (Raeburn et al., 2013; Zhao et al., 2015). Supramolecular
888 self-assemblies based on multiple noncovalent forces have emerged as an effective way to
889 fabricate multiple stimuli-responsive and self-healable intelligent hydrogels. Hectorite
890 nanoparticles and polymer can synergistically work together to produce a supramolecular hydrogel
891 with improved biological, chemical, mechanical and physical properties. In particular, recent
892 studies have indicated that such inorganic-organic hydrogels provide a biomimetic and hydrated
893 3D microenvironment (Annabi et al., 2014; Pedron, et al., 2015; Ma et al., 2018).

894 Hectorite nanoparticles form delaminated dispersions in water and self-assemble via
895 face-edge aggregation, creating an open, macroporous and thixotropic hydrogel network
896 (Takahashi et al., 2005). Nevertheless, hectorite nanoparticles is often used to improve the
897 mechanical properties of a supramolecular hydrogel. For example, Wang et al. (2010) reported a
898 kind of supramolecular nanocomposite hydrogel with high mechanical strength and a
899 fast-recovery capability. The hydrogel consisted of four components: water, hectorite nanolayers, a
900 dendritic macromolecule (Gn-binder) and sodium polyacrylate. The hydrogelation occurred by
901 kinetic trapping of the 3D network structure formed by the adhesion of G3-binder onto hectorite
902 nanolayers. The improved mechanical strength resulted largely from the mechanical toughness of
903 hectorite nanolayers. The hydrogel of poly(N-isopropylacrylamide) (PNIPAM) and hectorite with
904 a nacre-like brick-and mortar arrangement of organic and inorganic layers showed enhanced
905 mechanical properties and transparency (Wang et al., 2012). The noncovalent interactions between
906 hectorite and PNIPAM were hydrogen bonding between amide side groups (-CONH) on PNIPAM
907 and the surface SiOH or Si-O groups of the hectorite. The excellent mechanical properties were
908 attributed to the layered micro-/ nanoscale structure and the unique polymer/hectorite network.

909 Hectorite nanoparticles not only increased the strength of the hydrogel but also impacted the
910 toughness of the hydrogel. Organic-inorganic hybrid self-assemblies can not only enhance the
911 mechanical but also change optical properties of supramolecular hydrogels. Li et al. (2017a;
912 2017b; 2018) constructed self-supported supramolecular hydrogels through the hierarchically
913 organic-inorganic hybridization of hectorite matrix with organic ligands. The cooperative
914 interactions between the organic ligand parts and the negatively charged hectorite nanolayers

915 mainly contributed to connection of the organic and inorganic components to form the
916 supramolecular hydrogels. The luminescent supramolecular hydrogels consist of emitting sources,
917 organic ligand and hectorite are transparent, have self-healing properties and tunable mechanical
918 strength (Li et al., 2017a). Multifunctional nanocomposite gels consisting hectorite, isocyanate
919 (NCO)-terminated sP(EO-stat-PO) macromers, and clickable bicyclononynes (BCN) are
920 biocompatible, slowly degradable, and possess high mechanical strength (Topuz et al., 2017).
921 Even though the NCO-sP(EO-stat-PO) macromers could form a hydrogel network in water, the
922 incorporation of hectorite led to significant improvement of the mechanical properties.

923 Hydrogels have great potential for 3D printing. Remarkably, they can be rapidly printed into
924 complex 3D structures for cell culturing and tissue engineering (Kolesky et al., 2014). Hectorite
925 nanoparticles have been experimentally mixed with various responsive hydrogel precursors to
926 improve their 3D printability. Hong et al. (2015a) prepared the polyethylene glycol
927 (PEG)-alginate-hectorite hydrogels as the ink of a 3D printer. Hectorite significantly enhanced the
928 viscosity of PEG-alginate hydrogel and increased its shear-thinning properties. The hydrogels can
929 be printed into diverse shapes and suitable for long-term human mesenchymal stem cells (hMSC)
930 culture. More recently, hectorite was found to be an effective additive to improve the
931 self-supporting printability of N-isopropylacrylamide (NIPAAm), a thermoresponsive hydrogel
932 precursor (Jin et al., 2018). Therein graphene oxide (GO) was further added to respond to
933 near-infrared radiation and thus worked as a nanoscale heater (**Fig. 20**). Hectorite can be mixed
934 with these responsive hydrogel precursors of NIPAAm to improve their 3D printability. The
935 methodology pNIPAAm-hectorite-GO nanocomposite hydrogels can be further applied to prepare
936 various 3D printable responsive nanocomposite hydrogels.

937

938

Fig. 20.

939

940 Deoxyribonucleic acid (DNA) hydrogels are water-swollen 3D networks of DNA strands.
941 DNA hydrogels have such unique properties as biocompatibility, highly selective binding, and
942 molecular recognition. Nevertheless, DNA hydrogels suffer from poor mechanical properties and
943 low dimensional stability (Okay, 2011). Introducing hectorite into DNA hydrogels improves the

944 stability of DNA hydrogels due to the strong electrostatic interactions between DNA molecules
945 and the positively charged edges of hectorite (Arfin and Bohidar, 2013). Interconnecting linear
946 poly(N-isopropylacrylamide) chains, double-stranded(ds)-DNA strands, and hectorite
947 nanoparticles can form a 3D network of hydrogels (Uzumcu et al., 2016). Hectorite nanoparticles
948 acted as a multifunctional dynamic cross-linkers, and the non-covalent interactions made the
949 strong DNA hydrogels sensitivity to temperature. Uzumcu et al. (2018) recently prepared by in
950 situ polymerization of N,N-dimethylacrylamide (DMAA) in aqueous solution of
951 double-stranded(ds)-DNA (2-8 w/v %) in the presence of hectorite nanoparticles. The
952 DNA/hectorite hydrogel had high stretchability (up to 1500%) and a tensile strength between 20
953 and 150 kPa. Hectorite nanoparticles acted as a chemical cross-linker and promoted the elastic
954 behavior of the hydrogels, whereas DNA contributed to their viscoelastic energy dissipation.

955

956 **5.5. Biomedical materials**

957 Hectorite has great potential for drug vehicle, regenerative medicine and tissue engineering
958 (Hoppe et al., 2011). The swellability, delamination and the structure of “house-of-cards” of
959 hectorite makes it possible to host many biological and medical compounds. In particular,
960 hectorite hydrogels allows a one-step procedure for the encapsulation and delivery of drugs and
961 there is no need for tedious and costly chemical/physical process (Dawson et al., 2011). In
962 addition, hectorite nanolayers offers efficient affinities for protein-based antigen molecules via
963 electrostatic force (Dawson et al., 2011). Moreover, hectorite finally degrades into Na^+ , Mg^{2+} ,
964 Si(OH)_4 , Li^+ in aqueous solution (Wang et al., 2013). The ions are non-toxic to cell (Min et al.,
965 2014). For example, shear-thinning nanocomposite hydrogels of hectorite-gelatin were
966 biocompatible and biodegradable (Gaharwar et al., 2014). Once hectorite nanoparticles are taken
967 up by macrophage cells in the injection site, they may undergo biodegradation processes in the
968 late endosome and lysosome (Chen et al., 2016). Furthermore, the incorporation of hectorite
969 nanoparticles into nanocomposite hydrogels enhance mechanical properties. Hence, such
970 nanocomposite hydrogels can act better as 3D scaffolds for tissue engineering. For example, the
971 incorporation of hectorite nanoparticles into a poly (ethylene glycol) (PEG)–alginate hydrogel

972 significantly enhanced the compressive and tensile properties of the biocompatible hydrogel s
973 (Chang et al., 2010).

974 Hectorite can be used to prepare magnetic resonance imaging (MRI) contrast agents by
975 providing the colloidal stability for Fe_xO_y nanoparticles, a type of contrast agent. The
976 nanocomposite of hectorite and Fe_2O_3 had an improved relaxivity over mono-dispersed Fe_2O_3
977 nanoparticles (Tzitzios et al., 2010). Ding et al. (2016) developed a facile controlled
978 coprecipitation method to immobilized Fe_3O_4 on hectorite. The hectorite- Fe_3O_4 nanoparticles had
979 good water-dispersibility and colloidal stability, and can be metabolized and cleared out of the
980 body. Hectorite- Fe_3O_4 nanoparticles can not only be used as a contrast agent for magnetic
981 resonance imaging of cancer cells *in vitro* due to the effective uptake by tumor cells, but also
982 significantly enhanced the contrast of an xenografted tumor model.

983 A moldable nanocomposite hydrogel combining a mussel-inspired polymer,
984 dopamine-modified multiarmed polyethylene glycol (PEG-D) and hectorite was recently created
985 by Liu and Lee (2016). The interactions between polymer-bound dopamine and hectorite led to the
986 autoxidation of dopamine and the subsequent covalent cross-linking of catechol residues (Hong et
987 al., 2015b). The nanocomposite hydrogel acted as adhesive in biomedicine and can be used for
988 sealing tissue surfaces with a complex and non-flat geometry. A fit-to-shape sealant on the tissue
989 has been well made by combining dopamine-modified polyethylene glycol and hectorite, without
990 the use of cytotoxic oxidants to develop the moldable hydrogel (Liu et al., 2017). The hydrogel
991 transformed from a reversibly cross-linked network formed by dopamine-hectorite interfacial
992 interactions to a covalently cross-linked network through the slow autoxidation and cross-linking
993 of catechol moieties. The hydrogel can be remolded to different shapes. It also can be recovered
994 from large strain deformation, and can be injected through a syringe to adhere to the convex
995 contour of a tissue surface. With time, the hydrogel solidified to adopt the new shape and sealed
996 defects on the tissue. Such fit-to-shape sealant has great potential for sealing tissues with non-flat
997 geometries, such as a sutured anastomosis.

998 Delaminated hectorite nanoparticles form good dispersion in water and undergoes
999 self-assembly via face-edge aggregation creating an open, macroporous and thixotropic hydrogel
1000 network (Takahashi et al., 2005). The thixotropic properties of hectorite allow the establishment of

1001 a hydrogel network sufficiently cohesive to bridge gaps about 1cm (**Fig. 21a**). Adding
1002 pre-dispersed hectorite into electrolyte solutions generates gel capsules. The morphologies
1003 progressing from amorphous residues to discrete spherical capsules when physiological ionic
1004 strength (equivalent to 100–150 mM NaCl) is increased. Hectorite capsule formed in response to
1005 drop-wise addition to media of varying ionic strength (NaCl concentration) (**Fig. 21b**). Cells
1006 suspended in hectorite formulations of low viscosity were encapsulated by direct addition to cell
1007 culture media (**Fig. 21c**). The hectorite capsules had good cytocompatibility and can incorporate
1008 extra-cellular matrix molecules to modulate the behavior of encapsulated populations. Such
1009 hectorite capsules can stimulated angiogenesis *in vitro* and *in vivo* following a brief exposure to
1010 soluble vascular endothelial growth factor (**Fig. 21d**) (Dawson et al., 2011). The bioactive
1011 nanoparticles based on the interaction of hectorite nanoparticles with bone tissue at cellular levels
1012 was also revealed (Gaharwar et al., 2013). In the absence of any osteoinductive factor, the
1013 hectorite capsules promoted *in vitro* osteogenic differentiation of human mesenchymal stem cells
1014 (hMSCs) and such work open a possibility to use hectorite for coating bone-recovery materials.

1015

1016

Fig. 21.

1017

1018 Hectorite has been widely used in the pharmaceutical industry both as excipients and active
1019 substances (Carretero, 2002). The high anisotropy of electrostatic interaction enabled the
1020 encapsulation of drug molecules within the interlayer space of hectorite with a high retention
1021 capacity of drug (Takahashi et al., 2005). Hectorite-protein interaction has been harnessed in drug
1022 delivery to delay or localize therapeutic molecules through hydrophobic and interlamellar
1023 mechanisms. Besides, hectorite has a remarkable capacity for protein retention because the
1024 flocculation of hectorite nanoparticles in saline solutions enhance the adsorption of active
1025 molecules (Nennemann et al., 2001). When hectorite nanoparticles are dispersed in a drug solution,
1026 it can be recovered as a drug-clay solid phase and dried so that it can be made into tablets (Aguzzi
1027 et al., 2007). In addition, hectorite can help insoluble organic compounds to distribute well in
1028 water. For example, the hybridization of itraconazole (ITA)with hectorite can enhance water
1029 solubility and facilitate controlled release (Jung et al., 2008). In other words, hectorite can be used

1030 as a solubility controller or helper by the intercalation of organic drug molecules into the interlayer
1031 space of hectorite.

1032 Dox is a commonly used chemotherapeutic drugs but its efficacy is limited due to its low
1033 ability for tumor tissue penetration, insufficient cellular uptake and drug resistance. Through an
1034 ion exchange reaction, Dox was encapsulated into the interlayer space of hectorite with an
1035 exceptionally high loading efficiency of $98.3 \pm 0.77\%$ (Wang et al., 2013). Hectorite/Dox
1036 complexes also can act as a promising platform for tumor therapy (Li et al., 2014). Hectorite/Dox
1037 nanohydrogel allows to release the drug in the acidic environment of the endolysosome, and helps
1038 in disrupting the endolysosome. It was biocompatible and is cleared out of body after
1039 post-treatment for 45 d. Dox can also be encapsulated within hectorite/alginate hybrid
1040 nanocarriers (Gonçalves et al., 2014). Firstly, Dox was loaded onto biocompatible anionic
1041 hectorite nanolayers through strong electrostatic interactions to get DOX-loaded hectorite
1042 nanoparticles (**Fig. 22**). Then, alginate (AG) was coated onto the Dox-loaded hectorite
1043 nanoparticles (hectorite/Dox /AG nanohybrids) to prevent the burst release of the drug. The
1044 hectorite/Dox/AG nanohybrids had high encapsulation efficiency ($80.8 \pm 10.6\%$), were sensitive
1045 to pH, and displayed a sustained drug release behavior. The biocompatibility, high loading
1046 capacity and stimulus responsive release of cationic chemotherapeutic drugs of hectorite/alginate
1047 nanohybrids, make them excellent platforms for drug delivery. Targeting agents, such as folic acid
1048 (Wu et al., 2014) or lactobionic acid (Chen et al., 2015), were conjugated on the surface of
1049 hectorite. Lactobionic acid-modified hectorite and folic acid-modified hectorite proved to be able
1050 to encapsulate Dox with an efficiency of 91.5% and $92.1 \pm 2.2\%$, respectively. The modified
1051 hectorite can specifically deliver targeting agents to tumor cells and displayed targeted inhibition
1052 efficacy.

1053

1054

Fig. 22.

1055

1056 Besides, hectorite has been used for building hybrid theranostic nanoplatfoms. Zhuang et al.
1057 (2017) invented a hectorite-PLA-PEG-PEI-(Au⁰)₅₀-HA/Dox nanocomplexes which displayed
1058 good stability, high drug loading efficiency ($91.0 \pm 1.8\%$), and sustained drug release with a

1059 pH-sensitive manner. The combination of polyethylenimine (PEI) and hectorite takes the
1060 advantage of the ultrahigh drug loading efficiency of hectorite and the abundant amine groups on
1061 PEI for stabilizing Au NPs as computed tomography (CT) imaging contrasts and conjugating
1062 targeting agents. The nanomaterials significantly inhibit the growth of tumors and decrease the
1063 side-effect of Dox. They can also be used as a targeted contrast agent for CT imaging of tumors.
1064 More recently, Xu et al. (2018) developed a targeted therapeutic agent for photothermal and
1065 photodynamic treatment of cancer cells overexpressing integrin $\alpha\beta3$ (**Fig. 23**). Indocyanine green
1066 (ICG) was intercalated into the interlayer space of synthetic hectorite via an ion exchange reaction
1067 (**Fig. 23a**). Such encapsulation of ICG in hectorite increased the stability of ICG in solution, and
1068 the coating of polydopamine (PDA) on the surface of ICG/hectorite provided additional
1069 photothermal conversion efficacy, and facilitated the targeting modification of a nanoplatform (**Fig.**
1070 **23b**). Such ICG/hectorite–PDA–PEG–RGD nanoparticles showed a high encapsulation efficiency
1071 of 94.1% (**Fig. 23c**). These nanoparticles can specifically target at cancer cells overexpressing
1072 integrin $\alpha\beta3$, enhance cellular uptake and exert improved photothermal and photodynamic
1073 therapeutic effect on targeted cells upon Near Infrared(NIR) laser irradiation. In addition, Becher
1074 et al. (2018) prepared a nanohydrogel drug delivery platform consisting of hectorite nanolayers,
1075 polyacrylate, and sodium phosphate salts. The nanohydrogel was held by an outer shell of
1076 hectorite nanolayers aligned edge-to-edge probably intercalated with the polyacrylate polymer and
1077 sodium ions to balance the charges (**Fig. 24**). The guest molecules remained trapped in the
1078 tridimensional ionic hydrogel network during this process. The nanohydrogels appeared
1079 biocompatible, biodegradable, pH-responsive, and noncytotoxic. Such hydrogels are versatile
1080 platform because they e can simultaneously encapsulate several cancer drugs. Namely, they are an
1081 efficient drug cocktail delivery system and presents a positive synergistic effect.

1082

1083 **Fig. 23.**

1084

1085 **Fig. 24.**

1086

1087 **6. Summary and remarks**

1088 Hectorite, as an easily synthesized and gel-formed clay mineral, has captured particular
1089 attention of scientists and technologists since the middle of the 20th century. An upsurge of
1090 developing strategies for modification and new applications is seen in recent decades. Despite the
1091 fact that of hydrothermal synthesis of hectorite are well commercialized, new quicker and cleaner
1092 processes, typically melt solid-state reaction and continuously microfluidic synthesis, are
1093 emerging and needed, with an objective to better achieve. quicker delamination of synthetic
1094 hectorite and higher aspect ratio of hectorite nanolayers. During the process, the extent to which
1095 hectorite delaminate, the size of hectorite nanolayers or layer charge density of the hectorite and
1096 also modification will be finely controlled simultaneously.

1097 In addition to ion exchange, intercalation, and pillaring, many new strategies for modifying
1098 hectorite have now been developed. Surface engineering and tactic assembly of hectorite
1099 nanolayers allow many hectorite-based nanohybrids and hierarchical materials to be fabricated.
1100 Accordingly, the applications of hectorite have been significantly broaden. As well-defined 2D
1101 nanolayers, the assembly of hectorite nanoparticles with other molecules into functional films and
1102 membranes or hierarchical materials seems to be the most promising research topics. In this
1103 context, many nanoparticles and polymers have not been yet touched. Nevertheless, it should not
1104 be neglected that the conventional yet exclusively characteristics of hectorite, such as
1105 hydrogelation and thickening, rheological and thixotropic properties can be utilized in a wide
1106 range of fields and it worth further developing. Particularly, such features are essential in 3D
1107 printable ink materials and smart soft matter.

1108 In-depth understanding of physical and chemical properties of hectorite and new modification
1109 and assembly of hectorite nanoparticles are needed. In addition to adsorbents and catalysts,
1110 increasing concerns are about the uses of hectorite for making fluorescent reporters, biosensors,
1111 drug carriers and biomaterials for cell culture, tissue engineering and tumor therapy. Nevertheless,
1112 the insights into the functionality and inherent chemical and biological mechanism of
1113 hectorite-based materials *in vivo* remain in infancy and are still elusive. With the rapid
1114 development of cleaner synthesis process technology, tactic modification and assembly, the

1115 applications of the hectorite will be further expanded. Because synthetic hectorite possess
1116 exclusive nanostructure, nanoscale interlayer space and nanolayer, to use for surface plasmon
1117 resonance catalysts, biosensors, targeted drug vehicles, and tissue engineering materials could be
1118 new driving force to stimulate the expansion of synthetic hectorite in industry and related
1119 profitable marketplace in near future.

1120

1121

1122

1123 **Acknowledgments**

1124 The authors wish to acknowledge the financial support from the National Natural Scientific Foundation of China (41672033;
1125 21373185), the financial support by the open fund from Key Laboratory of Clay Minerals of Ministry of Land and Resources of
1126 the People's Republic of China, Engineering Research Center of Non-metallic Minerals of Zhejiang Province, Zhejiang Institute
1127 of Geology and Mineral Resource, China (ZD2018K04), and the State Key Laboratory Breeding Base of Green
1128 Chemistry-Preparation Technology, Zhejiang University of Technology (GCTKF2014006)

1129 **References**

- 1130 Aguzzi, C., Cerezo, P., Viseras, C., & Caramella, C. (2007). Use of clays as drug delivery systems:
1131 possibilities and limitations. *Applied Clay Science*, 36(1): 22-36.
- 1132 Annabi, N., Tamayol, A., Uquillas, J.A., Akbari, M., Bertassoni, L.E., Cha, C., Camci-Unal, G.,
1133 Dokmeci, M.R., Peppas, N.A. and Khademhosseini, A., 2014. 25th anniversary article: Rational
1134 design and applications of hydrogels in regenerative medicine. *Advanced Materials*, 26(1): 85.
- 1135 Arbeloa, F.L. and Martínez, V.M., 2011. Orientation of Adsorbed Dyes in the Interlayer Space of Clays.
1136 2 Fluorescence Polarization of Rhodamine 6G in Laponite Films. *Chemistry of Materials*, 18(6):
1137 393-5.
- 1138 Arfin, N. and Bohidar, H.B., 2013. Ergodic-to-nonergodic phase inversion and reentrant ergodicity
1139 transition in DNA-nanoclay dispersions. *Soft Matter*, 10(1): 149-156.

1140 Awad, W.H., Beyer, G., Benderly, D., Ijdo, W.L., Songtipya, P., Jimenez-Gasco, M.d.M., Manias, E.
1141 and Wilkie, C.A., 2009. Material properties of nanoclay PVC composites. *Polymer*, 50(8):
1142 1857-1867.

1143 Barick, A.K. and Tripathy, D.K., 2010. Preparation and characterization of thermoplastic
1144 polyurethane/organoclay nanocomposites by melt intercalation technique: Effect of nanoclay on
1145 morphology, mechanical, thermal, and rheological properties. *Journal of Applied Polymer
1146 Science*, 117(2): 639-654.

1147 Barker, R.M. and Jones, D.L., 1970. Chemistry of soil minerals. Part VIII. Synthesis and properties of
1148 fluorhectorites. *Journal of the Chemical Society A Inorganic Physical Theoretical*: 1531-1537.

1149 Barrer, R.M. and Dicks, L.W.R., 1967. Synthetic Alkylammonium Montmorillonites and Hectorites.
1150 *Journal of the Chemical Society A Inorganic Physical Theoretical*.

1151 Barrientos-Velázquez, A.L., Marroquin Cardona, A., Liu, L., Phillips, T. and Deng, Y., 2016. Influence
1152 of layer charge origin and layer charge density of smectites on their aflatoxin adsorption.
1153 *Applied Clay Science*, 132-133: 281-289.

1154 Baskaralingam, P., Pulikesi, M., Ramamurthi, V. and Sivanesan, S., 2007. Modified hectorites and
1155 adsorption studies of a reactive dye. *Applied Clay Science*, 37(1-2): 207-214.

1156 Bbosa, G.S., Kitya, D., Odda, J. and Ogwalokeng, J., 2013. Aflatoxins metabolism, effects on
1157 epigenetic mechanisms and their role in carcinogenesis. *Health*, 5(10A): 14-34.

1158 Becher, T.B., Mendonca, M.C.P., de Farias, M.A., Portugal, R.V., de Jesus, M.B. and Ornelas, C., 2018.
1159 Soft Nanohydrogels Based on Laponite Nanodiscs: A Versatile Drug Delivery Platform for
1160 Theranostics and Drug Cocktails. *ACS Appl Mater Interfaces*, 10(26): 21891-21900.

1161 Ben Zid, T., Fadhli, M., Khedher, I. and Fraile, J.M., 2017. New bis(oxazoline)-vanadyl complexes,
1162 supported by electrostatic interaction in Laponite clay, as heterogeneous catalysts for
1163 asymmetric oxidation of methyl phenyl sulfide. *Microporous and Mesoporous Materials*, 239:
1164 167-172.

1165 Bian, L., Song, M., Dong, F., Duan, T., Xu, J., Li, W. and Zhang, X., 2015. DFT and two-dimensional
1166 correlation analysis for evaluating the oxygen defect mechanism of low-density 4f (or 5f)
1167 elements interacting with ca-mt. *Rsc Advances*, 5(36): 28601-28610.

1168 Bickmore, B.R., Bosbach, D., Hochella, M.F., Charlet, L. and Rufe, E., 2001. In situ atomic force
1169 microscopy study of hectorite and nontronite dissolution: Implications for phyllosilicate edge
1170 surface structures and dissolution mechanisms. *American Mineralogist*, 86(4): 411-423.

1171 Borsacchi, S., Geppi, M., Ricci, L., Ruggeri, G. and Veracini, C.A., 2007. Interactions at the surface of
1172 organophilic-modified laponites: a multinuclear solid-state NMR study. *Langmuir the Acs*
1173 *Journal of Surfaces & Colloids*, 23(7): 3953.

1174 Bourlinos, A.B., And, D.D.J. and Giannelis, E.P., 2004. Clay–Organosiloxane Hybrids: A Route to
1175 Cross-Linked Clay Particles and Clay Monoliths. *Chemistry of Materials*, 16(12): 2404-2410.

1176 Bracco, S., Valsesia, P., Ferretti, L., Sozzani, P., Mauri, M. and Comotti, A., 2008. Spectroscopic
1177 observations of hybrid interfaces and gas storage in organo-clays. *Microporous and Mesoporous*
1178 *Materials*, 107(1-2): 102-107.

1179 Brandt, H., Bosbach, D., Panak, P.J. and Fanghänel, T., 2007. Structural incorporation of Cm(III) in
1180 trioctahedral smectite hectorite: A time-resolved laser fluorescence spectroscopy (TRLFS) study.
1181 *Geochimica Et Cosmochimica Acta*, 71(1): 145-154.

1182 Breen, C. and Komadel, P., 1995. Characterisation of moderately acid-treated, size-fractionated
1183 montmorillonites using IR and MAS NMR spectroscopy and thermal analysis. *Journal of*
1184 *Materials Chemistry*, 5(3): 469-474.

1185 Breu J., Seidl. W. and Stoll. A., 2003. Fehlordnung bei Smectiten in Abhängigkeit vom
1186 Zwischenschichtkation. *Zeitschrift Für Anorganische Und Allgemeine Chemie*, 629(3): 503-515.

1187 Buck, M.E., Zhang, J. and Lynn, D.M., 2007. Layer-by-Layer Assembly of Reactive Ultrathin Films
1188 Mediated by Click-Type Reactions of Poly(2-Alkenyl Azlactone)s. *Advanced Materials*, 19(22):
1189 3951-3955.

1190 Carrado, K.A., 2000. Synthetic organo- and polymer–clays: preparation, characterization, and materials
1191 applications. *Applied Clay Science*, 17(1–2): 1-23.

1192 Carrado, K.A., Csencsits, R., Thiyagarajan, P., Seifert, S., Macha, S.M. and Harwood, J.S., 2002.
1193 Crystallization and textural porosity of synthetic clay minerals. *Journal of Materials Chemistry*,
1194 12(11): 3228-3237.

1195 Carrado, K.A., Thiyagarajan, P. and Song, K., 1997. A study of organo-hectorite clay crystallization.
1196 *Clay Minerals*, 32(1): 29-40.

1197 Carrado, K.A., Xu, L., D.M.G., K. Song, S. Seifert, A. and Botto, R.E., 2015. Crystallization of a
1198 Layered Silicate Clay as Monitored by Small-Angle X-ray Scattering and NMR. *Chemistry of*
1199 *Materials*, 12(10): 3052-3059.

1200 Carretero, M. I. (2002). Clay minerals and their beneficial effects upon human health. a review.
1201 *Applied Clay Science*, 21(3): 155-163.

1202 Chang, C.W., Spreeuwel, A.V., Zhang, C. and Varghese, S., 2010. PEG/clay nanocomposite hydrogel: a
1203 mechanically robust tissue engineering scaffold. *Soft Matter*, 6(20): 5157-5164.

1204 Chen, G., Li, D., Li, J., Cao, X., Wang, J., Shi, X. and Guo, R., 2015. Targeted doxorubicin delivery to
1205 hepatocarcinoma cells by lactobionic acid-modified laponite nanodisks. *New Journal of*
1206 *Chemistry*, 39(4): 2847-2855.

1207 Chen, W., Zhang, B., Mahony, T., Gu, W., Rolfe, B. and Xu, Z.P., 2016. Efficient and Durable Vaccine
1208 against Intimin β of Diarrheagenic E. Coli Induced by Clay Nanoparticles. *Small*, 12(12): 1627.

1209 Christidis, G. , Aldana, C. , Chryssikos, G. , Gionis, V. , Kalo, H. , Stöter, M., Breu, J., and Robert J.,
1210 2018. The nature of laponite: pure hectorite or a mixture of different trioctahedral phases?
1211 *Minerals*, 8(8).

1212 Cho, K.L., Hill, A.J., Caruso, F. and Kentish, S.E., 2015. Chlorine resistant glutaraldehyde crosslinked
1213 polyelectrolyte multilayer membranes for desalination. *Advanced Materials*, 27(17): 2791.

1214 Contin, A., Biffis, A., Sterchele, S., Dormbach, K., Schipmann, S. and Pich, A., 2014. Metal
1215 nanoparticles inside microgel/clay nanohybrids: Synthesis, characterization and catalytic
1216 efficiency in cross-coupling reactions. *J Colloid Interface Sci*, 414: 41-5.

1217 Cool, P. and Vansant, E.F., 1996. Preparation and characterization of zirconium pillared laponite and
1218 hectorite. *Microporous Materials*, 6(1): 27-36.

1219 Cummins, H.Z., 2007. Liquid, glass, gel: The phases of colloidal Laponite. *Journal of Non-Crystalline*
1220 *Solids*, 353(41-43): 3891-3905.

1221 Daab, M., Rosenfeldt, S., Kalo, H., Stöter, M., Bojer, B., Siegel, R., Forster, S., Senker, J. and Breu, J.,
1222 2017. Two-Step Delamination of Highly Charged, Vermiculite-like Layered Silicates via
1223 Ordered Heterostructures. *Langmuir*, 33(19): 4816-4822.

1224 Daniel, L.M., Frost, R.L. and Zhu, H.Y., 2008. Edge-modification of laponite with
1225 dimethyl-octylmethoxysilane. *J Colloid Interface Sci*, 321(2): 302-9.

1226 Dawson, J.I., Kanczler, J.M., Yang, X.B., Attard, G.S. and Oreffo, R.O., 2011. Clay gels for the
1227 delivery of regenerative microenvironments. *Adv Mater*, 23(29): 3304-8.

1228 Dawson, J.I. and Oreffo, R.O., 2013. Clay: new opportunities for tissue regeneration and biomaterial
1229 design. *Adv Mater*, 25(30): 4069-86.

1230 Decarreau, A., Grauby, O., & Petit, S. (1992). The actual distribution of octahedral cations in 2: 1 clay
1231 minerals: results from clay synthesis. *Applied Clay Science*, 7(1-3), 147-167.

1232 Decarreau, A., Vigier, N., Palkova, H., Petit, S., Vieillard, P. and Fontaine, C., 2012. Partitioning of
1233 lithium between smectite and solution: An experimental approach. *Geochimica et*
1234 *Cosmochimica Acta*, 85: 314-325.

1235 Decarreau A. 1980. Experimental crystallogenesi of Mg-smectite:hectorite, stevensite. *Bull. Minéral.*
1236 103:579-590.

1237 Deepracha, S., Bureekaew, S., & Ogawa, M., 2019. Synergy effects of the complexation of a titania and
1238 a smectite on the film formation and its photocatalyst'performance. *Applied Clay Science*, 169,
1239 129-134.

1240 Delavernhe, L., Pilavtepe, M. and Emmerich, K., 2018. Cation exchange capacity of natural and
1241 synthetic hectorite. *Applied Clay Science*, 151: 175-180.

1242 Dimos, K., Arcudi, F., Kouloumpis, A., Koutselas, I.B., Rudolf, P., Gournis, D. and Prato, M., 2017.
1243 Top-down and bottom-up approaches to transparent, flexible and luminescent nitrogen-doped
1244 carbon nanodot-clay hybrid films. *Nanoscale*, 9(29): 10256-10262.

1245 Ding, L., Hu, Y., Luo, Y., Zhu, J., Wu, Y., Yu, Z., Cao, X., Peng, C., Shi, X. and Guo, R., 2016.
1246 LAPONITE(R)-stabilized iron oxide nanoparticles for in vivo MR imaging of tumors. *Biomater*
1247 *Sci*, 4(3): 474-82.

1248 Duque-Redondo, E., Manzano, H., Epelde-Elezcano, N., Martínez-Martínez, V. and López-Arbeloa, I.,
1249 2014. Molecular Forces Governing Shear and Tensile Failure in Clay-Dye Hybrid Materials.
1250 *Chemistry of Materials*, 26(15): 4338-4345.

1251 Dykes, L.M.C., Torkelson, J.M., Burghardt, W.R. and Krishnamoorti, R., 2010. Shear-induced
1252 orientation in polymer/clay dispersions via in situ X-ray scattering. *Polymer*, 51(21): 4916-4927.

1253 Elder, D.L., Benight, S.J., Song, J., Robinson, B.H. and Dalton, L.R., 2014. Matrix-Assisted Poling of
1254 Monolithic Bridge-Disubstituted Organic NLO Chromophores. *Chemistry of Materials*, 26(2):
1255 872–874.

1256 Fenero, M., Palenzuela, J., Azpitarte, I., Knez, M., Rodriguez, J. and Tena-Zaera, R., 2017.
1257 Laponite-Based Surfaces with Holistic Self-Cleaning Functionality by Combining Antistatics
1258 and Omniphobicity. *ACS Appl Mater Interfaces*, 9(44): 39078-39085.

1259 Finck, N., Dardenne, K. and Geckeis, H., 2015. Am(III) coprecipitation with and adsorption on the
1260 smectite hectorite. *Chemical Geology*, 409: 12-19.

1261 Finck, N., Stumpf, T., Walther, C. and Bosbach, D., 2008. TRLFS characterization of Eu(III)-doped
1262 synthetic organo-hectorite. *Journal of Contaminant Hydrology*, 102(3–4): 253-262.

1263 Franco, F., Pozo, M., Cecilia, J.A., Benítez-Guerrero, M. and Lorente, M., 2016. Effectiveness of
1264 microwave assisted acid treatment on dioctahedral and trioctahedral smectites. The influence of
1265 octahedral composition. *Applied Clay Science*, 120: 70-80.

1266 Fujimura, T., Ramasamy, E., Ishida, Y., Shimada, T., Takagi, S. and Ramamurthy, V., 2016. Sequential
1267 energy and electron transfer in a three-component system aligned on a clay nanosheet. *Physical
1268 Chemistry Chemical Physics Pccp*, 18(7): 5404.

1269 Gaharwar, A.K., Avery, R.K., Assmann, A., Paul, A., Mckinley, G.H., Khademhosseini, A. and Olsen,
1270 B.D., 2014. Shear-thinning nanocomposite hydrogels for the treatment of hemorrhage. *Acs
1271 Nano*, 8(10): 9833.

1272 Gaharwar, A.K., Mihaila, S.M., Swami, A., Patel, A., Sant, S., Reis, R.L., Marques, A.P., Gomes, M.E.
1273 and Khademhosseini, A., 2013. Bioactive silicate nanoplatelets for osteogenic differentiation of
1274 human mesenchymal stem cells. *Adv Mater*, 25(24): 3329-36.

1275 Gao, R., Fang, X. and Yan, D., 2018. Direct white-light emitting room-temperature-phosphorescence
1276 thin films with tunable two-color polarized emission through orientational hydrogen-bonding
1277 layer-by-layer assembly. *Journal of Materials Chemistry C*, 6(16): 4444-4449.

1278 Gonçalves, M., Figueira, P., Maciel, D., Rodrigues, J., Qu, X., Liu, C., Tomás, H. and Li, Y., 2014.
1279 pH-sensitive Laponite®/doxorubicin/alginate nanohybrids with improved anticancer efficacy.
1280 *Acta Biomaterialia*, 10(1): 300-7.

1281 González, B., da Silva, T.H., Ciuffi, K.J., Vicente, M.A., Trujillano, R., Rives, V., de Faria, E.H., Korili,
1282 S.A. and Gil, A., 2017. Laponite functionalized with biuret and melamine-Application to
1283 adsorption of antibiotic trimethoprim. *Microporous and Mesoporous Materials*, 253: 112-122.

1284 Grabolle, M., Starke, M. and Resch-Genger, U., 2016. Highly Fluorescent dye-nanoclay Hybrid
1285 Materials Made from Different Dye Classes. *Langmuir*, 32(14): 3506-13.

1286 Guerra, D.L., Airoidi, C., Lemos, V.P. and Angelica, R.S., 2008. Adsorptive, thermodynamic and
1287 kinetic performances of Al/Ti and Al/Zr-pillared clays from the Brazilian Amazon region for
1288 zinc cation removal. *J Hazard Mater*, 155(1-2): 230-42.

1289 Guerra, D.L., Airoidi, C. and Viana, R.R., 2010. Modification of hectorite by organofunctionalization
1290 for use in removing U(VI) from aqueous media: thermodynamic approach. *J Environ Radioact*,
1291 101(2): 122-33.

1292 Guerra, D.L., Santos, M.R.M.C. and Airoidi, C., 2009. Mercury adsorption on natural and
1293 organofunctionalized smectites - thermodynamics of cation removal. *Journal of the Brazilian
1294 Chemical Society*, 20(20): 594-603.

1295 Hai, C., Zhou, Y., Fuji, M., Shirai, T., Ren, X., Zeng, J. and Li, X., 2018a. Electrical conductivity of
1296 hydrothermally synthesized sodium lithium magnesium silicate. *Materials Research Bulletin*, 97:
1297 473-482.

1298 Hai, C., Zhou, Y., Wang, F. and Fuji, M., 2018b. Direct growth of lithium magnesium silicate
1299 nanotubes on a glass slide. *CrystEngComm*, 20(32): 4694-4701.

1300 Hashimoto, K., Irie, H., & Fujishima, A., 2005. TiO₂ photocatalysis: a historical overview and future
1301 prospects. *Japanese Journal of Applied Physics*, 44(12), 8269-8285.

1302 Hegyesi, N., Vad, R.T. and Pukánszky, B., 2017. Determination of the specific surface area of layered
1303 silicates by methylene blue adsorption: The role of structure, pH and layer charge. *Applied Clay
1304 Science*, 146: 50-55.

1305 Heinz, H., Vaia, R.A., Krishnamoorti, R., & Farmer, B. L., 2007. Self-Assembly of Alkylammonium
1306 Chains on Montmorillonite: Effect of Chain Length, Head Group Structure, and Cation
1307 Exchange Capacity. *Chemistry of Materials*, 19(1): 59-68.

1308 Herling, M.M., Kalo, H., Seibt, S., Schobert, R. and Breu, J., 2012. Tailoring the pore sizes of
1309 microporous pillared interlayered clays through layer charge reduction. *Langmuir*, 28(41):
1310 14713-9.

1311 Higashi, S., Miki, H. and Komarneni, S., 2007. Mn-smectites: Hydrothermal synthesis and
1312 characterization. *Applied Clay Science*, 38(1-2): 104-112.

1313 Hill, E.H., Claes, N., Bals, S. and Liz-Marzán, L.M., 2016. Layered Silicate Clays as Templates for
1314 Anisotropic Gold Nanoparticle Growth. *Chemistry of Materials*, 28(14): 5131-5139.

1315 Hill, E.H., Zhang, Y. and Whitten, D.G., 2015. Aggregation of cationic p-phenylene ethynyls on
1316 Laponite clay in aqueous dispersions and solid films. *J Colloid Interface Sci*, 449: 347-56.

1317 Hong, S., Sycks, D., Chan, H.F., Lin, S., Lopez, G.P., Guilak, F., Leong, K.W. and Zhao, X., 2015a. 3D
1318 Printing of Highly Stretchable and Tough Hydrogels into Complex, Cellularized Structures. *Adv*
1319 *Mater*, 27(27): 4035-40.

1320 Hong, S.H., Shin, M., Lee, J., Ryu, J.H., Lee, S., Yang, J.W., Kim, W.D. and Lee, H., 2015b. Stable
1321 Alginate Gel Prepared by Linkage Exchange from Ionic to Covalent Bonds. *Advanced*
1322 *Healthcare Materials*, 5(1): 75-79.

1323 Hoppe, A., Gldal, N.S. and Boccaccini, A.R., 2011. A review of the biological response to ionic
1324 dissolution products from bioactive glasses and glass-ceramics. *Biomaterials*, 32(11): 2757-74.

1325 Huang, X., Ivanova, N., Strzelec, A. and Zacharia, N.S., 2018. Assembly of large area crack free clay
1326 porous films. *RSC Advances*, 8(2): 1001-1004.

1327 Iwasaki, T., 1989. Rheological Properties of Organophilic Synthetic Hectorites and Saponites. *Clays &*
1328 *Clay Minerals*, 37(3): 248-257.

1329 Iwase, H. , Ogura, T. , Sakuma, H. , Tamura, K. , & Fukushima, Y. . 2018. Structural investigation of
1330 hectorite aqueous suspensions by dielectric microscopy and small-angle neutron scattering
1331 coupling with rheological measurement. *Applied Clay Science*, 157: 24-30.

1332 Jaber, M. and Mieh -Brendl , J., 2008. Synthesis, characterization and applications of 2:1
1333 phyllosilicates and organophyllosilicates: Contribution of fluoride to study the octahedral sheet.
1334 *Microporous and Mesoporous Materials*, 107(1-2): 121-127.

1335 Ji, Y., Xie, W., Fan, Y., Shi, Y., Kong, D. and Lu, J., 2016. Degradation of trimethoprim by
1336 thermo-activated persulfate oxidation: Reaction kinetics and transformation mechanisms.
1337 Chemical Engineering Journal, 286: 16-24.

1338 Jin, Y., Shen, Y., Yin, J., Qian, J. and Huang, Y., 2018. Nanoclay-Based Self-Supporting Responsive
1339 Nanocomposite Hydrogels for Printing Applications. ACS Appl Mater Interfaces, 10(12):
1340 10461-10470.

1341 Josef, B., Seidl, W., Alexander J. Stoll, and, K.G.L. and Probst, T.U., 2001. Charge Homogeneity in
1342 Synthetic Fluorohectorite. Chem. Mater(13): 4213-4220.

1343 Joshi, G.V., Pawar, R.R., Kevadiya, B.D. and Bajaj, H.C., 2011. Mesoporous synthetic hectorites: A
1344 versatile layered host with drug delivery application. Microporous and Mesoporous Materials,
1345 142(2-3): 542-548.

1346 Jung, H., Kim, H. Y., Hwang, S., & Choy, J. (2008). Laponite-based nanohybrid for enhanced solubility
1347 and controlled release of itraconazole. Int J Pharm, 349(1), 283-290.

1348 Kalo, H., Milius, W. and Breu, J., 2012a. Single crystal structure refinement of one- and two-layer
1349 hydrates of sodium fluorohectorite. RSC Advances, 2(22): 8452.

1350 Kalo, H., Moller, M.W., Kunz, D.A. and Breu, J., 2012b. How to maximize the aspect ratio of clay
1351 nanoplatelets. Nanoscale, 4(18): 5633-9.

1352 Kalo, H., Möller, M.W., Ziadeh, M., Dolejš, D. and Breu, J., 2010. Large scale melt synthesis in an
1353 open crucible of Na-fluorohectorite with superb charge homogeneity and particle size. Applied
1354 Clay Science, 48(1-2): 39-45.

1355 Karmous, M.S., Ben Rhaïem, H., Robert, J.L., Lanson, B. and Ben Haj Amara, A., 2009. Charge
1356 location effect on the hydration properties of synthetic saponite and hectorite saturated by Na⁺,
1357 Ca²⁺ cations: XRD investigation. Applied Clay Science, 46(1): 43-50.

1358 Keeling, J. L., and Zhou, C. H., 2012. Clay research opportunities arising from increased trade between
1359 china and south australia. China Non-Metallic Minerals Industry.

1360 Khan, F.-A., Vallat, A. and Süß-Fink, G., 2011. Highly selective low-temperature hydrogenation of
1361 furfuryl alcohol to tetrahydrofurfuryl alcohol catalysed by hectorite-supported ruthenium
1362 nanoparticles. Catalysis Communications, 12(15): 1428-1431.

1363 Khan, F.-A., Vallat, A. and Süß-Fink, G., 2012. Highly selective C=C bond hydrogenation in
1364 α,β -unsaturated ketones catalyzed by hectorite-supported ruthenium nanoparticles. *Journal of*
1365 *Molecular Catalysis A: Chemical*, 355: 168-173.

1366 Kolesky, D. B. , Truby, R. L. , Gladman, A. S. , Busbee, T. A. , Homan, K. A. , & Lewis, J. A.. 2014.
1367 3D bioprinting of vascularized, heterogeneous cell-laden tissue constructs. *Advanced Materials*,
1368 26(19): 3124-3130.

1369 Komadel, P., 2016. Acid activated clays: Materials in continuous demand. *Applied Clay Science*, 131:
1370 84-99.

1371 Komadel, P., Janek, M., Madejová, J., Weekes, A. and Breen, C., 1997. Acidity and catalytic activity of
1372 mildly acid-treated Mg-rich montmorillonite and hectorite. *J.chem.soc.faraday Trans*, 93(23):
1373 4207-4210.

1374 Kotal, M. and Bhowmick, A.K., 2015. Polymer nanocomposites from modified clays: Recent advances
1375 and challenges. *Progress in Polymer Science*, 51: 127-187.

1376 Lee B , Koo S., 2011. Preparation of silver nanoparticles on the surface of fine magnetite particles by a
1377 chemical reduction[J]. *Journal of Industrial & Engineering Chemistry*, 17(4):762-766.

1378 Ley, C., Bordat, P., di Stefano, L.H., Remongin, L., Ibrahim, A., Jacques, P. and Allonas, X., 2015a.
1379 Joint spectroscopic and theoretical investigation of cationic cyanine dye Astrazon Orange-R:
1380 solvent viscosity controlled relaxation of excited states. *Phys Chem Chem Phys*, 17(8): 5982-90.

1381 Ley, C., Brendle, J., Miranda, M. and Allonas, X., 2017. Spectroscopic Studies of the Interactions
1382 between a Cationic Cyanine Dye and a Synthetic Phyllosilicate: From Photophysics to Hybrid
1383 Materials. *Langmuir*, 33(27): 6812-6818.

1384 Ley, C., Brendle, J., Walter, A., Jacques, P., Ibrahim, A. and Allonas, X., 2015b. On the interaction of
1385 triarylmethane dye crystal violet with LAPONITE(R) clay: using mineral nanoparticles to
1386 control the dye photophysics. *Phys Chem Chem Phys*, 17(26): 16677-81.

1387 Lezhnina, M.M., Grewe, T., Stoehr, H. and Kynast, U., 2012. Laponite Blue: Dissolving the Insoluble.
1388 *Angewandte Chemie International Edition*, 51(42): 10652-10655.

1389 Li, K., Wang, S., Wen, S., Tang, Y., Li, J., Shi, X. and Zhao, Q., 2014. Enhanced In Vivo Antitumor
1390 Efficacy of Doxorubicin Encapsulated within Laponite Nanodisks. *ACS Applied Materials &*
1391 *Interfaces*, 6(15): 12328-12334.

1392 Li, Z., Hou, Z., Fan, H. and Li, H., 2017a. Organic-Inorganic Hierarchical Self-Assembly into Robust
1393 Luminescent Supramolecular Hydrogel. *Advanced Functional Materials*, 27(2): 1604379.

1394 Li, Z., Li, P., Xu, Q., and Li, H., 2015. Europium(III)- β -diketonate complex-containing nanohybrid
1395 luminescent pH detector. *Chemical Communications*, 51(53): 10644-7.

1396 Li, Z., Wang, G., Wang, Y. and Li, H., 2018. Reversible Phase Transition of Robust Luminescent
1397 Hybrid Hydrogels. *Angew Chem Int Ed Engl*, 57(8): 2194-2198.

1398 Li, Z., Zhang, Y.-M., Wang, H.-Y., Li, H. and Liu, Y., 2017b. Mechanical Behaviors of Highly Swollen
1399 Supramolecular Hydrogels Mediated by Pseudorotaxanes. *Macromolecules*, 50(3): 1141-1146.

1400 Liu, H., Gu, X., Hu, M., Hu, Y. and Wang, C., 2014a. Facile fabrication of nanocomposite
1401 microcapsules by combining layer-by-layer self-assembly and Pickering emulsion templating.
1402 *RSC Adv.*, 4(32): 16751-16758.

1403 Liu, J., Liu, G., Zhang, M., Sun, P. and Zhao, H., 2013. Synthesis and Self-Assembly of Amphiphilic
1404 Janus Laponite Disks. *Macromolecules*, 46(15): 5974-5984.

1405 Liu, L.F., Cai, Z.B., Shen, J.N., Wu, L.X., Hoek, E.M.V. and Gao, C.J., 2014b. Fabrication and
1406 characterization of a novel poly(amide-urethane@imide) TFC reverse osmosis membrane with
1407 chlorine-tolerant property. *Journal of Membrane Science*, 469(6): 397-409.

1408 Liu, Y. and Lee, B.P., 2016. Recovery property of double-network hydrogel containing mussel-inspired
1409 adhesive moiety and nano-silicate. *Journal of Materials Chemistry B Materials for Biology &*
1410 *Medicine*, 4(40): 6534-6540.

1411 Liu, Y., Meng, H., Qian, Z., Fan, N., Choi, W., Zhao, F. and Lee, B.P., 2017. A moldable nanocomposite
1412 hydrogel composed of a mussel-inspired polymer and a nanosilicate as a fit-to-shape tissue
1413 sealant. *Angew Chem Int Ed Engl*, 56(15): 4224-4228.

1414 Ma, J., Jia, Y., Jing, Y., Sun, J. and Yao, Y., 2009. Synthesis and photocatalytic activity of
1415 TiO₂-hectorite composites. *Applied Clay Science*, 46(1): 114-116.

1416 Ma, Y., Lin, M., Huang, G., Li, Y., Wang, S., Bai, G., Lu, T., and Xu, F. 2018. 3D Spatiotemporal
1417 Mechanical Microenvironment: A Hydrogel- Based Platform for Guiding Stem Cell Fate.
1418 *Advanced Materials*, 30(49): 1705911.

1419 Makoto, O., Takayuki, M. and Tomohiko, O., 2008. Preparation of hectorite-like swelling silicate with
1420 controlled layer charge density. *Journal of the Ceramic Society of Japan*.

1421 Min, J., Braatz, R.D. and Hammond, P.T., 2014. Tunable staged release of therapeutics from
1422 layer-by-layer coatings with clay interlayer barrier. *Biomaterials*, 35(8): 2507-17.

1423 Mishra, A.K., Chattopadhyay, S., Rajamohanan, P.R. and Nando, G.B., 2011. Effect of tethering on the
1424 structure-property relationship of TPU-dual modified Laponite clay nanocomposites prepared by
1425 ex-situ and in-situ techniques. *Polymer*, 52(4): 1071-1083.

1426 Möller, M.W., Hirsemann, D., Haarmann, F., Senker, J.r. and Breu, J., 2010. Facile Scalable Synthesis
1427 of Rectorites. *Chemistry of Materials*, 22(1): 186-196.

1428 Muller, F., Besson, G., Manceau, A. and Drits, V.A., 1997. Distribution of isomorphous cations within
1429 octahedral sheets in montmorillonite from Camp-Bertaux. *Physics & Chemistry of Minerals*,
1430 24(3): 159-166.

1431 Naveau, E., Calberg, C., Detrembleur, C., Bourbigot, S., Jérôme, C. and Alexandre, M., 2009.
1432 Supercritical CO₂ as an efficient medium for layered silicate organomodification: Preparation of
1433 thermally stable organoclays and dispersion in polyamide 6. *Polymer*, 50(6): 1438-1446.

1434 Nennemann, A., Kulbach, S. and Lagaly, G., 2001. Entrapping pesticides by coagulating smectites.
1435 *Applied Clay Science*, 18(5): 285-298.

1436 Norma, N.H., Jeanmarie, L., Jeanluc, P., Laurent, D. and Elodie, B., 2004. Aqueous Dispersions of
1437 Silane-Functionalized Laponite Clay Platelets. A First Step toward the Elaboration of
1438 Water-Based Polymer/Clay Nanocomposites. *Langmuir*, 20(5): 1564-1571.

1439 Okada T., Matsutomo T., and Ogawa M., 2010. Nanospace Engineering of Methylviologen Modified
1440 Hectorite-Like Layered Silicates with Varied Layer Charge Density for the Adsorbents Design. *J.*
1441 *Phys. Chem. C*, 539-545.

1442 Okada, T., Kobari, H. and Haeiwa, T., 2016a. Effects of fluoride and urea on the crystal growth of a
1443 hectorite-like layered silicate on a silica surface. *Applied Clay Science*, 132-133: 320-325.

1444 Okada, T., Kumasaki, A., Shimizu, K., Yamagishi, A. and Sato, H., 2016b. Application of
1445 Hectorite-Coated Silica Gel Particles as a Packing Material for Chromatographic Resolution. *J*
1446 *Chromatogr Sci*, 54(7): 1238-43.

1447 Okada, T. and Ogawa, M., 2003. 1,1'-Dimethyl-4,4'-bipyridinium-smectites as a novel adsorbent of
1448 phenols from water through charge-transfer interactions. *Chemical Communications*, 9(12):
1449 1378.

1450 Okada, T., Sueyoshi, M. and Minamisawa, H.M., 2015a. In Situ Crystallization of Al-Containing
1451 Silicate Nanosheets on Monodisperse Amorphous Silica Microspheres. *Langmuir*, 31(51):
1452 13842-9.

1453 Okada, T., Suzuki, A., Yoshido, S. and Minamisawa, H.M., 2015b. Crystal architectures of a layered
1454 silicate on monodisperse spherical silica particles cause the topochemical expansion of the
1455 core-shell particles. *Microporous and Mesoporous Materials*, 215: 168-174.

1456 Okada, T., Yoshido, S., Miura, H., Yamakami, T., Sakai, T. and Mishima, S., 2012. Swellable
1457 Microsphere of a Layered Silicate Produced by Using Monodispersed Silica Particles. *The*
1458 *Journal of Physical Chemistry C*, 116(41): 21864-21869.

1459 Okay, O., 2011. DNA hydrogels: New functional soft materials. *Journal of Polymer Science Part B*
1460 *Polymer Physics*, 49(8): 551-556.

1461 Osman, A.F., Edwards, G.A., Schiller, T.L., Andriani, Y., Jack, K.S., Morrow, I.C., Halley, P.J. and
1462 Martin, D.J., 2012. Structure–Property Relationships in Biomedical Thermoplastic Polyurethane
1463 Nanocomposites. *Macromolecules*, 45(1): 198-210.

1464 Pardhy, N.P. and Budhlall, B.M., 2010. Pickering emulsion as a template to synthesize Janus colloids
1465 with anisotropy in the surface potential. *Langmuir*, 26(16): 13130-41.

1466 Patro, T.U. and Wagner, H.D., 2011. Layer-by-layer assembled PVA/Laponite multilayer free-standing
1467 films and their mechanical and thermal properties. *Nanotechnology*, 22(45): 455706.

1468 Patro, T.U. and Wagner, H.D., 2016. Influence of graphene oxide incorporation and chemical
1469 cross-linking on structure and mechanical properties of layer-by-layer assembled poly(Vinyl
1470 alcohol)-Laponite free-standing films. *Journal of Polymer Science Part B: Polymer Physics*,
1471 54(22): 2377-2387.

1472 Pawar, R.R., Kevadiya, B.D., Brahmabhatt, H. and Bajaj, H.C., 2013. Template free synthesis of
1473 mesoporous hectorites: efficient host for pH responsive drug delivery. *Int J Pharm*, 446(1-2):
1474 145-52.

1475 Pawar, R.R., Lalmunsiam, Gupta, P., Sawant, S.Y., Shahmoradi, B. and Lee, S.M., 2018. Porous
1476 synthetic hectorite clay-alginate composite beads for effective adsorption of methylene blue dye
1477 from aqueous solution. *International Journal of Biological Macromolecules*, 114: 1315.

1478 Pawar, R.R., Patel, H.A., Sethia, G. and Bajaj, H.C., 2009. Selective adsorption of carbon dioxide over
1479 nitrogen on calcined synthetic hectorites with tailor-made porosity. *Applied Clay Science*, 46(1):
1480 109-113.

1481 Petit S., Righi D., Decarreau A. 2008. Transformation of synthetic Zn-stevensite to Zn-talc induced by
1482 the Hofmann-Klemen effect. *Clays and Clay Min.*, 56, 645-654.

1483 Pedron, S., Becka, E., & Harley, B. A. 2015. Spatially gradated hydrogel platform as a 3D engineered
1484 tumor microenvironment. *Advanced Materials*, 27(9): 1567-1572.

1485 Phothitontimongkol, T., Sanuwong, K., Siebers, N., Sukpirom, N. and Unob, F., 2013. Functionalized
1486 hectorite clay mineral for Ag(I) ions extraction from wastewater and preparation of silver
1487 nanoparticles supported clay. *Applied Clay Science*, 80-81: 346-350.

1488 Phothitontimongkol, T., Siebers, N., Sukpirom, N. and Unob, F., 2009. Preparation and characterization
1489 of novel organo-clay minerals for Hg(II) ions adsorption from aqueous solution. *Applied Clay
1490 Science*, 43(3-4): 343-349.

1491 Phuoc, T.X., Howard, B.H. and Chyu, M.K., 2009. Synthesis and rheological properties of
1492 cation-exchanged Laponite suspensions. *Colloids and Surfaces A: Physicochemical and
1493 Engineering Aspects*, 351(1-3): 71-77.

1494 Priolo, M.A., Holder, K.M., Greenlee, S.M., Stevens, B.E. and Grunlan, J.C., 2013. Precisely Tuning
1495 the Clay Spacing in Nanobrick Wall Gas Barrier Thin Films. *Chemistry of Materials*, 25(9):
1496 1649-1655.

1497 Pujala, R.K., Schneijdenberg, C., van Blaaderen, A. and Bohidar, H.B., 2018. In-situ Observation of
1498 Hierarchical Self-Assembly Driven by Bicontinuous Gelation in Mixed Nanodisc Dispersions.
1499 *Sci Rep*, 8(1): 5589.

1500 Raeburn, J., Zamith, C.A. and Adams, D.J., 2013. The importance of the self-assembly process to
1501 control mechanical properties of low molecular weight hydrogels. *Chemical Society Reviews*,
1502 42(12): 5143-56.

1503 Rajesh, S., Zhao, Y., Fong, H. and Menkhaus, T.J., 2017. Nanofiber multilayer membranes with
1504 tailored nanochannels prepared by molecular layer-by-layer assembly for high throughput
1505 separation. *J. Mater. Chem. A*, 5(9): 4616-4628.

1506 Robertson, J. and Bandosz, T.J., 2006. Photooxidation of dibenzothiophene on TiO₂/hectorite thin
1507 films layered catalyst. *J Colloid Interface Sci*, 299(1): 125-35.

1508 Sánchez, T., Gebretsadik, F.B., Salagre, P., Cesteros, Y., Guillén-Hurtado, N., García-García, A. and
1509 Bueno-López, A., 2013a. Evaluation of hectorites, synthesized in different conditions, as soot
1510 combustion catalysts after impregnation with copper. *Applied Clay Science*, 77-78: 40-45.

1511 Sánchez, T., Salagre, P. and Cesteros, Y., 2013b. Ultrasounds and microwave-assisted synthesis of
1512 mesoporous hectorites. *Microporous and Mesoporous Materials*, 171: 24-34.

1513 Sánchez, T., Salagre, P., Cesteros, Y. and Bueno-López, A., 2012. Use of delaminated hectorites as
1514 supports of copper catalysts for the hydrogenolysis of glycerol to 1,2-propanediol. *Chemical
1515 Engineering Journal*, 179: 302-311.

1516 Sawant, S.Y., Pawar, R.R., Somani, R.S. and Bajaj, H.C., 2014. Facile hard template approach for
1517 synthetic hectorite hollow microspheres. *Materials Letters*, 128: 121-124.

1518 Schoonheydt, R.A., 1991. Clay Adsorbed Dyes: Methylene Blue on Laponite. *Clay Minerals*, 27(1):
1519 91-100.

1520 Sethia, G., Patel, H.A., Pawar, R.R. and Bajaj, H.C., 2014. Porous synthetic hectorites for selective
1521 adsorption of carbon dioxide over nitrogen, methane, carbon monoxide and oxygen. *Applied
1522 Clay Science*, 91-92: 63-69.

1523 Shi, L., Xu, Y. and Li, Q., 2008. Controlled Growth of Lead Oxide Nanosheets, Scrolled Nanotubes,
1524 and Nanorods. *Crystal Growth & Design*, 8(10): 3521-3525.

1525 Spagnuolo, M., 2004. Coprecipitation of trace metal ions during the synthesis of hectorite. *Applied
1526 Clay Science*, 27(3-4): 129-140.

1527 Staniford, M.C., Lezhnina, M.M., Gruener, M., Stegemann, L., Kuczius, R., Bleicher, V., Strassert, C.A.
1528 and Kynast, U.H., 2015. Photophysical efficiency-boost of aqueous aluminium phthalocyanine
1529 by hybrid formation with nano-clays. *Chemical Communications*, 51(70): 13534-13537.

1530 Stocker, M., Seidl, W., Seyfarth, L., Senker, J. and Breu, J., 2008. Realisation of truly microporous
1531 pillared clays. *Chem Commun (Camb)*(5): 629-31.

1532 Storaro, L., Lenarda, M., Ganzerla, R. and Rinaldi, A., 1996. Preparation of hydroxy Al and Al/Fe
1533 pillared bentonites from concentrated clay suspensions. *Microporous Materials*, 6(2): 55-63.

1534 Stöter, M., Biersack, B., Reimer, N., Herling, M., Stock, N., Schobert, R. and Breu, J., 2014. Ordered
1535 Heterostructures of Two Strictly Alternating Types of Nanoreactors. *Chemistry of Materials*,
1536 26(18): 5412-5419.

1537 Stöter, M., Biersack, B., Rosenfeldt, S., Leitl, M.J., Kalo, H., Schobert, R., Yersin, H., Ozin, G.A.,
1538 Förster, S. and Breu, J., 2015. Encapsulation of functional organic compounds in nanoglass for
1539 optically anisotropic coatings. *Angewandte Chemie*, 54(16): 4963-7.

1540 Stöter, M., Godrich, S., Feicht, P., Rosenfeldt, S., Thurn, H., Neubauer, J.W., Seuss, M., Lindner, P.,
1541 Kalo, H., Moller, M., Fery, A., Förster, S., Papastavrou, G. and Breu, J., 2016. Controlled
1542 Exfoliation of Layered Silicate Heterostructures into Bilayers and Their Conversion into Giant
1543 Janus Platelets. *Angew Chem Int Ed Engl*, 55(26): 7398-402.

1544 Stöter, M., Kunz, D.A., Schmidt, M., Hirsemann, D., Kalo, H., Putz, B., Senker, J. and Breu, J., 2013.
1545 Nanoplatelets of sodium hectorite showing aspect ratios of approximately 20,000 and superior
1546 purity. *Langmuir*, 29(4): 1280-5.

1547 Strese, H. and Hofmann, U., 1941. Synthese von Magnesiumsilikat-Gelen mit zweidimensional
1548 regelmässiger struktur. *Zeitschrift Für Anorganische Und Allgemeine Chemie*, 247.

1549 Such, G.K., Quinn, J.F., Quinn, A., Tjipto, E. and Caruso, F., 2006. Assembly of ultrathin polymer
1550 multilayer films by click chemistry. *Journal of the American Chemical Society*, 128(29):
1551 9318-9319.

1552 Sudha, J.D., Pich, A., Reena, V.L., Sivakala, S. and Adler, H.-J.P., 2011. Water-dispersible
1553 multifunctional polyaniline-laponite-keggin iron nanocomposites through a template approach.
1554 *Journal of Materials Chemistry*, 21(41): 16642.

1555 Sun, B., Khan, F.-A., Vallat, A. and Süss-Fink, G., 2013. NanoRu@hectorite: A heterogeneous catalyst
1556 with switchable selectivity for the hydrogenation of quinoline. *Applied Catalysis A: General*,
1557 467: 310-314.

1558 Süss-Fink, G., Khan, F.A., Boudon, J. and Spassov, V., 2009. Shape- and Size-Selective Preparation of
1559 Hectorite-Supported Ruthenium Nanoparticles for the Catalytic Hydrogenation of Benzene.
1560 *Journal of Cluster Science*, 20(2): 341-353.

- 1561 Süss-Fink, G., Mollwitz, B., Therrien, B., Dadras, M., Laurency, G., Meister, A. and Meister, G., 2006.
1562 Ruthenium Nanoparticles Intercalated in Hectorite: A Reusable Hydrogenation Catalyst for
1563 Benzene and Toluene. *Journal of Cluster Science*, 18(1): 87-95.
- 1564 Suzuki, Y., Tenma, Y., Nishioka, Y., Kamada, K., Ohta, K. and Kawamata, J., 2011. Efficient
1565 Two-Photon Absorption Materials Consisting of Cationic Dyes and Clay Minerals. *Journal of*
1566 *Physical Chemistry C*, 115(42): 20653–20661.
- 1567 Szöllösi, G., Gombkötő, D., Mogyorós, A.Z. and Fülöp, F., 2018. Surface-Improved Asymmetric
1568 Michael Addition Catalyzed by Amino Acids Adsorbed on Laponite. *Advanced Synthesis &*
1569 *Catalysis*, 360(10): 1992-2004.
- 1570 Takagi, S., Shimada, T., Ishida, Y., Fujimura, T., Masui, D., Tachibana, H., Eguchi, M. and Inoue, H.,
1571 2013. Size-matching effect on inorganic nanosheets: control of distance, alignment, and
1572 orientation of molecular adsorption as a bottom-up methodology for nanomaterials. *Langmuir*
1573 *the Acs Journal of Surfaces & Colloids*, 29(7): 2108-19.
- 1574 Takahashi, T., Yamada, Y., Kataoka, K. and Nagasaki, Y., 2005. Preparation of a novel PEG-clay hybrid
1575 as a DDS material: dispersion stability and sustained release profiles. *Journal of Controlled*
1576 *Release Official Journal of the Controlled Release Society*, 107(3): 408-16.
- 1577 Tan, H., Liu, W., Yu, D., Li, H., Hubbe, M.A., Gong, B., Zhang, W., Wang, H. and Li, G., 2014.
1578 ASA-in-water emulsions stabilized by laponite nanoparticles modified with
1579 tetramethylammonium chloride. *Chemical Engineering Science*, 116: 682-693.
- 1580 Tang, Y., Hill, E. H., Zhou, Z., Evans, D. G., Schanze, K. S., & Whitten, D. G. (2011). Synthesis,
1581 self-assembly, and photophysical properties of cationic oligo(p-phenyleneethynylene)s.
1582 *Langmuir*, 27(8), 4945-4955.
- 1583 Thien, B., Godon, N., Hubert, F. and Angéli, F., 2010. Structural identification of a trioctahedral
1584 smectite formed by the aqueous alteration of a nuclear glass. *Applied Clay Science*, 49(3):
1585 135-141.
- 1586 Tkáč, I., 1994. Acid-Treated Montmorillonites—A Study by ²⁹Si and ²⁷Al MAS NMR. *Clay Minerals*,
1587 29(1): 11-19.

1588 Tokieda, D., Tsukamoto, T., Ishida, Y., Ichihara, H., Shimada, T. and Takagi, S., 2017. Unique
1589 fluorescence behavior of dyes on the clay minerals surface: Surface Fixation Induced Emission
1590 (S-FIE). *Journal of Photochemistry & Photobiology A Chemistry*, 339: 67-79.

1591 Tomohiko, O. , Mutsuki, O. , Kazuki, T. , Tomohiko, Y. , & Hisako, S., 2018. Variation in thickness of a
1592 layered silicate on spherical silica particles affected hplc chiral chromatographic resolution.
1593 *Applied Clay Science*, 163:72-80.

1594 Topuz, F. , Bartneck, M. , Pan, Y. , & Tacke, F. . 2017. One-step fabrication of biocompatible
1595 multifaceted nanocomposite gels and nanolayers. *Biomacromolecules*, 18(2): 386-397.

1596 Trikittiwong, P., Sukpirom, N., Shimazu, S. and Chavasiri, W., 2014. Iron oxide-pillared clay catalyzed
1597 the synthesis of acetonides from epoxides. *Catalysis Communications*, 54: 104-107.

1598 Tsapatsis, M. and Maheshwari, S., 2008. Pores by pillaring: not always a maze. *Angew Chem Int Ed*
1599 *Engl*, 47(23): 4262-3.

1600 Tsukamoto, T., Shimada, T. and Takagi, S., 2015. Structure resembling effect of clay surface on
1601 photochemical properties of meso-phenyl or pyridyl-substituted monocationic antimony(V)
1602 porphyrin derivatives. *Rsc Advances*, 5(11): 8479-8485.

1603 Tzitzios, V., Basina, G., Bakandritsos, A., Hadjipanayis, C.G., Mao, H., Niarchos, D., Hadjipanayis,
1604 G.C., Tucek, J. and Zboril, R., 2010. Immobilization of magnetic iron oxide nanoparticles on
1605 laponite discs – an easy way to biocompatible ferrofluids and ferrogels. *Journal of Materials*
1606 *Chemistry*, 20(26): 5418-5428.

1607 Uzumcu, A.T., Guney, O. and Okay, O., 2016. Nanocomposite DNA hydrogels with temperature
1608 sensitivity. *Polymer*, 100: 169-178.

1609 Uzumcu, A.T., Guney, O. and Okay, O., 2018. Highly Stretchable DNA/Clay Hydrogels with
1610 Self-Healing Ability. *ACS Appl Mater Interfaces*, 10(9): 8296-8306.

1611 Varade, D. and Haraguchi, K., 2014. Novel bimetallic core-shell nanocrystal-clay composites with
1612 superior catalytic activities. *Chem Commun (Camb)*, 50(23): 3014-7.

1613 Velasco, J.I., Antunes, M., Ayyad, O., López-Cuesta, J.M., Gaudon, P., Saiz-Arroyo, C.,
1614 Rodríguez-Pérez, M.A. and Saja, J.A.D., 2007. Foaming behaviour and cellular structure of
1615 LDPE/hectorite nanocomposites. *Polymer*, 48(7): 2098-2108.

1616 Vicente, I., Salagre, P. and Cesteros, Y., 2010. Preparation of pure hectorite using microwaves. *Physics*
1617 *Procedia*, 8: 88-93.

1618 Vicente, I., Salagre, P., Cesteros, Y., Guirado, F., Medina, F. and Sueiras, J., 2009. Fast microwave
1619 synthesis of hectorite. *Applied Clay Science*, 43(1): 103-107.

1620 Wagner, H.D., 2007. Nanocomposites: paving the way to stronger materials. *Nature Nanotechnology*,
1621 2(12): 742-4.

1622 Wang, B., Zhou, M., Rozynek, Z. and Fossum, J.O., 2009. Electrorheological properties of organically
1623 modified nanolayered laponite: influence of intercalation, adsorption and wettability. *Journal of*
1624 *Materials Chemistry*, 19(13): 1816.

1625 Wang, J., Lin, L., Cheng, Q. and Jiang, L., 2012. A strong bio-inspired layered PNIPAM-clay
1626 nanocomposite hydrogel. *Angew Chem Int Ed Engl*, 51(19): 4676-80.

1627 Wang, J., Wheeler, P.A., Jarrett, W.L. and Mathias, L.J., 2007. Synthesis and characterization of dual-
1628 functionalized laponite clay for acrylic nanocomposites. *Journal of Applied Polymer Science*,
1629 106(3): 1496-1506.

1630 Wang, Q., Mynar, J.L., Yoshida, M., Lee, E., Lee, M., Okuro, K., Kinbara, K. and Aida, T., 2010.
1631 High-water-content mouldable hydrogels by mixing clay and a dendritic molecular binder.
1632 *Nature*, 463(7279): 339-43.

1633 Wang, S., Wu, Y., Guo, R., Huang, Y., Wen, S., Shen, M., Wang, J. and Shi, X., 2013. Laponite
1634 nanodisks as an efficient platform for Doxorubicin delivery to cancer cells. *Langmuir*, 29(16):
1635 5030-6.

1636 Wheeler, P.A., Wang, J., James Baker, A. and Mathias, L.J., 2005. Synthesis and Characterization of
1637 Covalently Functionalized Laponite Clay. *Chemistry of Materials*, 17(11): 3012-3018.

1638 Wu, Y., Guo, R., Wen, S., Shen, M., Zhu, M., Wang, J. and Shi, X., 2014. Folic acid-modified laponite
1639 nanodisks for targeted anticancer drug delivery. *J. Mater. Chem. B*, 2(42): 7410-7418.

1640 Xiao, S., Castro, R., Maciel, D., Goncalves, M., Shi, X., Rodrigues, J. and Tomas, H., 2016. Fine
1641 tuning of the pH-sensitivity of laponite-doxorubicin nanohybrids by polyelectrolyte multilayer
1642 coating. *Mater Sci Eng C Mater Biol Appl*, 60: 348-356.

1643 Xu, F., Liu, M., Li, X., Xiong, Z., Cao, X., Shi, X. and Guo, R., 2018. Loading of Indocyanine Green
1644 within Polydopamine-Coated Laponite Nanodisks for Targeted Cancer Photothermal and
1645 Photodynamic Therapy. *Nanomaterials (Basel)*, 8(5).

1646 Yang, Y., Liu, Z., Wu, D., Wu, M., Tian, Y., Niu, Z. and Huang, Y., 2013. Edge-modified amphiphilic
1647 Laponite nano-discs for stabilizing Pickering emulsions. *J Colloid Interface Sci*, 410: 27-32.

1648 Yang, Y. and Zhang, J., 2018. Highly Stable Lithium-Sulfur Batteries Based on Laponite
1649 Nanosheet-Coated Celgard Separators. *Advanced Energy Materials*, 8(25): 1801778.

1650 Yang, X. , Ke, X. , Yang, D. , Liu, J. , Guo, C. , Frost, R. , Su, H. , Zhu, H. , 2010. Effect of ethanol
1651 washing of titania clay mineral composites on photocatalysis for phenol decomposition. *Applied*
1652 *Clay Science*, 49(1-2), 0-50.

1653 Yao, Y., Jia, Y.Z., Sun, J.H., Jing, Y., Li, W., The method of using natural brine to synthesize
1654 magnesium lithium silicate montmorillonite. Patent Number: ZL 200510096406.5

1655 Yoon, K., Hsiao, B.S. and Chu, B., 2008. Functional nanofibers for environmental applications. *Journal*
1656 *of Materials Chemistry*, 18(44): 5326-5334.

1657 Yu, L. and Cebe, P., 2009. Crystal polymorphism in electrospun composite nanofibers of
1658 poly(vinylidene fluoride) with nanoclay. *Polymer*, 50(9): 2133-2141.

1659 Yu, W. H., Ren, Q. Q., Tong, D. S., Zhou, C. H., & Hao, W. 2014. Clean production of
1660 ctab-montmorillonite: formation mechanism and swelling behavior in xylene. *Applied Clay*
1661 *Science*, 97-98(8), 222-234.

1662 Yue, D., Jing, Y., Ma, J., Xia, C., Yin, X. and Jia, Y., 2011. Removal of Neutral Red from aqueous
1663 solution by using modified hectorite. *Desalination*, 267(1): 9-15.

1664 Yurekli, K., Conley, E. and Krishnamoorti, R., 2005. Effect of Laponite and a nonionic polymer on the
1665 absorption character of cationic dye solutions. *Langmuir the Acs Journal of Surfaces & Colloids*,
1666 21(13): 5825-30.

1667 Zhang, D., Zhou, C. H., Lin, C. X., Tong, D. S., & Yu, W. H. 2010. Synthesis of clay minerals. *Applied*
1668 *Clay Science*, 50(1), 0-11.

1669 Zhao, L.Z., Zhou, C.H., Wang, J., Tong, D.S., Yu, W.H. and Wang, H., 2015. Recent advances in clay
1670 mineral-containing nanocomposite hydrogels. *Soft Matter*, 11(48): 9229-46.

1671 Zhou, C. H. , Tong, D. , & Li, X. . 2010. Synthetic Hectorite: Preparation, Pillaring and Applications in
1672 Catalysis. Pillared Clays and Related Catalysts. Springer New York.

1673 Zhu, H. Y. , Zhao, J. C. , Liu, J. W. , Yang, X. Z. , & Shen, Y. N. , 2006. General synthesis of a
1674 mesoporous composite of metal oxide and silicate nanoparticles from a metal salt and laponite
1675 suspension for catalysis. Chemistry of Materials, 18(17), 3993-4001.

1676 Zhu, H. Y., Orthman, J. A., Li, J. Y., Zhao, J. C., Churchman, G. J., & Vansant, E. F., 2002. Novel
1677 composites of TiO₂ (anatase) and silicate nanoparticles. Chemistry of materials, 14(12),
1678 5037-5044.

1679 Zhuang, Y., Zhao, L., Zheng, L., Hu, Y., Ding, L., Li, X., Liu, C., Zhao, J., Shi, X. and Guo, R., 2017.
1680 LAPONITE-Polyethylenimine Based Theranostic Nanoplatform for Tumor-Targeting CT
1681 Imaging and Chemotherapy. ACS Biomaterials Science & Engineering, 3(3): 431-442.

1682

1683

1684

1685